

صدرت لأول مرة عام ١٩٥٦

مجلة

# المهندس

ISSN 2413 - 0230

المجلد ١٥٦ - العدد الرابع - كانون الأول ٢٠١٩

عدد خاص لبحوث المؤتمر الأول للأنظمة الحديثة في  
الهندسة الكهربائية والميكانيكية وتطبيقاتها - الجزء الثالث

مجلة علمية محكمة

تصدرها

جمعية المهندسين العراقية

(تأسست عام ١٩٣٨)



# مجلة المهندس

المجلد ١٥٦ – العدد الرابع – كانون الأول ٢٠١٩



جمعية المهندسين العراقية

## مجلة المهندس

مجلة المهندس هي مجلة علمية فصلية محكمة تعنى بالبحوث الهندسية تصدرها جمعية المهندسين العراقية (ISE) كنسخة مطبوعة وكذلك على الإنترنت. صدرت المجلة لأول مرة في عام ١٩٥٦.

الرقم الدولي المعياري ISSN: 2413-0230

حقوق الطبع والنشر © ٢٠١٩ من قبل جمعية المهندسين العراقية (ISE)

عنوان المكتب: العراق ، بغداد ، حي النضال - محلة ١٠٣ - شارع ٣٠ - بناية ٥

ص ب: ١٨٤٢٩

الهاتف: (+964) 7901803967 / (+964) 7901151092 / (+964) 7702526721

على الانترنت: [www.jmise.ise-iq.org](http://www.jmise.ise-iq.org)

البريد الإلكتروني: [jmise@ise-iq.org](mailto:jmise@ise-iq.org)

الاشتراك داخل العراق: ١٠٠٠٠٠٠ ألف دينار في السنة

الاشتراك خارج العراق: ٦٠٠ دولار في السنة

رقم الايداع في المكتبة الوطنية ببغداد ٥١٠ لسنة ١٩٨٣

## الرؤى والاهداف

مجلة المهندس هي مجلة علمية فصلية ، تغطي جميع أنواع البحوث العلمية في العديد من المجالات الهندسية مثل: الهندسة المدنية ، هندسة البناء والانشاءات ، الهندسة المعمارية ، الهندسة الميكانيكية ، الهندسة الكهربائية ، هندسة الاتصالات ، هندسة الحاسوب ، الهندسة الكيميائية ، هندسة النفط ، هندسة البيئة ، هندسة المواد ، هندسة الموارد المائية ، فضلا عن الحقول الهندسية الأخرى. تقدم المجلة منصة قوية للمهندسين العراقيين لنشر الأعمال التي تترجم معارفهم وخبراتهم ومهاراتهم.

## اخلاقيات النشر

تقبل المجلة تقديم أي أعمال بحثية تتناول المجالات الهندسية المختلفة، سواء المنهجية منها أو التطبيقية. يرجى من الباحثين إرسال اعمالهم البحثية بحيث لا تزيد عدد الصفحات عن ١٥ صفحة للبحث، وباستخدام برنامج MS Word ضمن قالب القياسي. يتم تطبيق مجموعة من الاجراءات لغرض الحصول على قبول النشر. وهذه الاجراءات هي:

- قبول الباحثين
- التحقق من المعايير
- التحقق من الاقتباس او الانتحال
- التحقق من عدم تكرار المنشور
- التحقق من الاستغلال
- التحقق من سوء التصرف
- ان يكون المنشور مقروء للجمهور الدولي (على الأقل العنوان والمستخلص باللغة الإنجليزية).
- التقييم العلمي المحكم
- موافقة هيئة التحرير

ان هيئة التحرير تسعى الى اكمال هذه الاجراءات خلال مدة لا تتجاوز (١٠) أسابيع من تاريخ تقديم البحث. يجب أن يحتوي البحث المقدم على ما يأتي: (١) اسم المجلة ، (٢) عنوان البحث ، (٣) اسم المؤلف (المؤلفين) ؛ (٤) المستخلص ؛ (٥) الكلمات الدالة ؛ (٦) نص البحث ؛ (٧) المراجع.

## جمعية المهندسين العراقية

تأسست جمعية المهندسين العراقية (ISE) في عام ١٩٣٨ من قبل مجموعة من المهندسين العراقيين الرواد. وقد تم تعيين ٣٦ هيئة إدارية منذ تشكيلها حتى الآن. ازداد عدد الاعضاء بمرور الزمن ليصل الى أكثر من ٤٠٠٠ عضو مؤخرًا. لدى الجمعية العديد من الهيئات النوعية التخصصية واللجان للإشراف والقيام بأنشطة علمية وهندسية وثقافية بشكل مستمر من أجل دعم المهندسين العراقيين بالخبرات والمهارات المطلوبة. تسعى الجمعية الى تحقيق أهدافها من خلال:

١. تنظيم المؤتمرات والندوات العلمية والمساهمة فيها.
٢. تنظيم دورات التعليم المستمر في الحقل الهندسي.
٣. تنظيم المحاضرات والمنشورات العلمية والثقافية.
٤. دعم وتشجيع البحوث والدراسات الهندسية.
٥. تنظيم الزيارات العلمية.
٦. جمع وتوثيق المعلومات العلمية والهندسية.
٧. تقديم الخبرة والاستشارات العلمية والهندسية.

## الهيئة الادارية

- المهندس الاستشاري فالح كاظم زاير/ رئيس الجمعية ورئيس الهيئة الادارية
- أ.د. حسين يوسف محمود/ نائب رئيس الجمعية
- المهندس الاستشاري علي حسين صبيح العلق/ امين السر
- المهندس محمد فاروق عبد الخالق/ الامين المالي
- أ.م.د. ماهر يحيى سلوم/ عضو
- د. فالح حمزة الربيعي/ عضو
- م.د. حيدر عامر احمد البغدادي/ عضو
- م. احمد صالح الزهيري/ عضو
- المهندس الاستشاري رياض كتاب حسين/ عضو
- المهندس الاستشاري حمودي خضير محمد/ عضو
- المهندس عبد اللطيف عبد الحسين صنكور/ عضو
- المهندس الاستشاري عبد السلام عبد الحسن الجشعمي/ عضو

## هيئة التحرير

- أ.د. حسين يوسف محمود، جامعة بغداد، كلية الهندسة/ رئيس هيئة التحرير
- أ.د. نجدت نشأت عبد الله ، جامعة البلقاء التطبيقية
- أ.د. غادة موسى رزوقي، جامعة بغداد ، كلية الهندسة
- أ.د. محمد زكي الفائز ، جامعة الفراهيدي
- أ. ماهر خضير محمود العزاوي ، الجامعة المستنصرية ، كلية الهندسة
- أ.م.د. سميرة محمد حمد الله ، جامعة بغداد ، كلية الهندسة
- أ.م.د. أحمد زيدان محمد الشمري ، جامعة بغداد ، كلية الهندسة الخوارزمي
- أ.م.د. نصير عبود الحبوبى ، جامعة النهريين ، كلية الهندسة
- أ.م.د. معن سلمان حسن ، الجامعة التكنولوجية ، قسم الهندسة المدنية
- أ.م.د. توفيق وسمي محمد ، الجامعة المستنصرية ، كلية الهندسة
- م.د. اميل محمد رحمن المياح، جامعة بغداد ، كلية الهندسة الخوارزمي
- م.د. باسم عبد الرزاق رشيد، جامعة بغداد ، كلية الهندسة

## الاستشاريون

- الأستاذ الدكتور أمين دواي التميمي
- الأستاذ الدكتور ماجد حميد مجيد
- الأستاذ الدكتور مظفر صادق الزهيري
- الأستاذ الدكتور قاسم جبار سليمان/ أستاذ في الهندسة الكيماوية
- الأستاذ الدكتور رامي حكمت فؤاد الحديثي/ أستاذ في الجامعة الاردنية
- الأستاذ الدكتور إحسان فتحي/ أستاذ في الهندسة المعمارية في جامعة فيلادلفيا الامريكية
- الأستاذ الدكتور خالد السلطاني/ أستاذ في الهندسة المعمارية في الدنمارك



# AL- MUHANDIS

Journal (JMISE)

Established in 1956

ISSN 2413 - 0230

Volume 156, Issue 4, December 2019

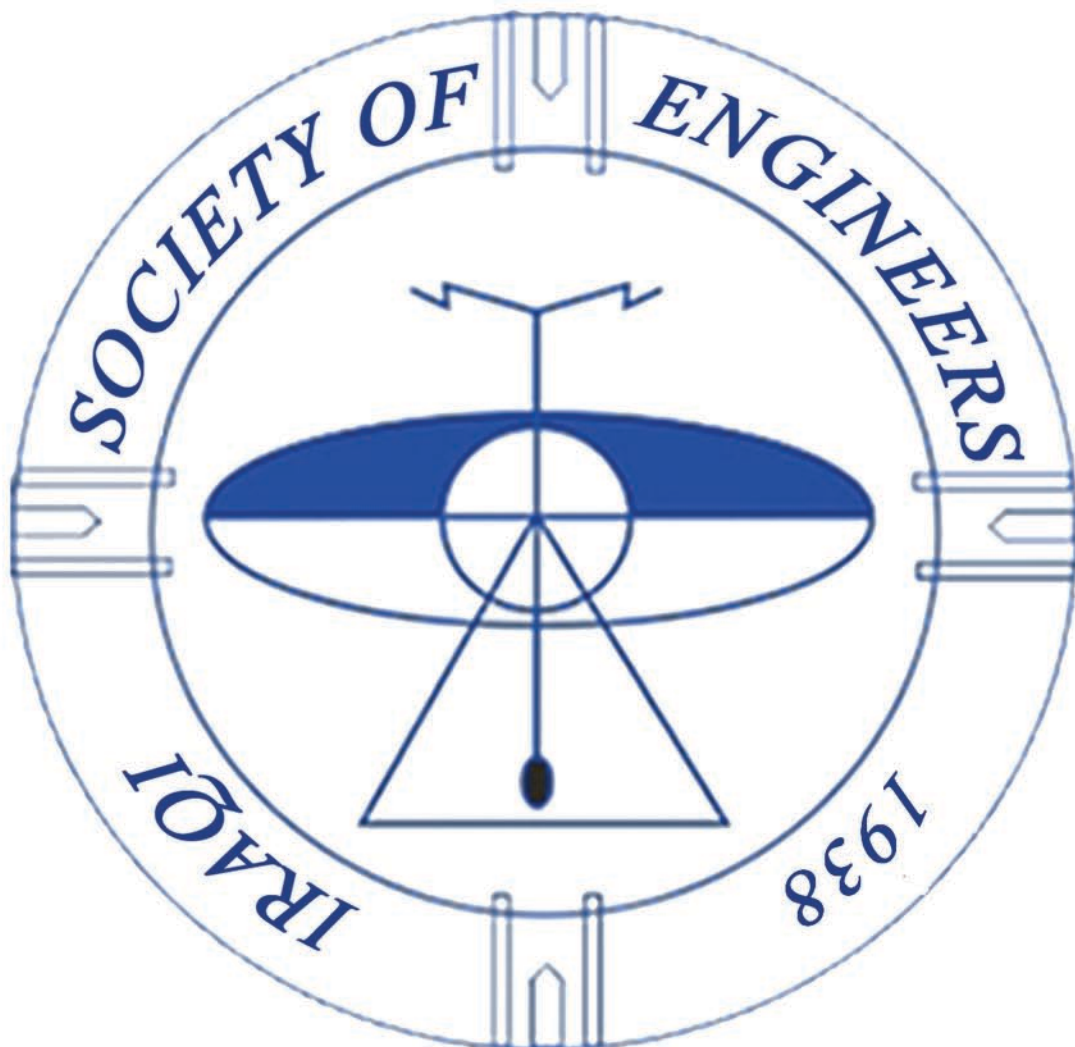
**Special Issue for the First Conference on Modern  
Electrical, Mechanical Engineering Systems and  
Applications - Part 3**

**Peer-Reviewed Scientific Journal**

**Published by**

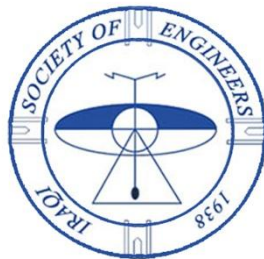
**Iraqi Society of Engineers (ISE)**

**Founded in 1938**



# **Al-MUHANDIS Journal (JMISE)**

**Volume 156, Issue 4, December 2019**



**Iraqi Society of Engineers**

## Publication Information

Al-MUHANDIS Journal (JMISE) is a seasonal scientific publication releases by the Iraqi Society of Engineers (ISE) as a hard copy as well as online. The journal has established for the first time in 1956.

ISSN: 2413-0230

Copyright © 2019 by Iraqi Society of Engineers (ISE)

Office Address: Iraq, Baghdad, Al-Nidhal Q., 103-30-5

P.O. Box: 18429

Mob: (+964) 7702526721 / (+964) 7901151092 / (+964) 7901803967

Online: [www.jmise.ise-iq.org](http://www.jmise.ise-iq.org)

E-mail: [jmise@ise-iq.org](mailto:jmise@ise-iq.org)

Subscription: 100000 ID Per Year in Iraq

\$600 per year for other countries

## Aims and Scope

Al-MUHANDIS Journal (JMISE) is a peer-reviewed scientific journal, covers all sorts of scientific researches in many engineering fields like: Civil and Construction, Architectural, Mechanical, Electrical, Communications, Computer, Chemical, Petroleum, Environmental, Materials, Water Resources as well as other engineering interests. The journal offers a solid platform for Iraqi engineers to publish works which translate their knowledge, expertise and skills.

# Publication Ethics

The journal accepts the submission of any research work deals with engineering fields, either methodology and/or applications. Prospective authors are invited to submit their draft manuscript in a short paper (no more than 15 pages) using MS Word format. The manuscripts should be processed through many steps in order to get acceptance. These processes are:

- Authorship satisfaction
- Standards validation
- Plagiarism complaints
- Anti- duplicatepublication
- Anti-misappropriation
- Malpractice statement
- Readable for international audiences (at least titles and abstracts in English).
- Peer reviewing
- Editorial acceptance

The target is that the process for each submitted manuscript should complete within (10) weeks from its submission. All papers should include: (1) Name of the journal, (2) Title of the manuscript, (3) Name and affiliation for the author(s); (4) Abstract; (5) Keywords; (6)Text of the manuscript; (7) References.

## Iraqi Society of Engineers

Iraqi society of engineers (ISE) has founded in 1938 by a group of leading Iraqi engineers. ISE has been assigned 36 administration commissions since its formation up to date. The number of members has been grown up from several members during its declaration to more than 4,000 members recently. ISE has several committees and boards to operate scientific, engineering and cultural activities continuously in order to support Iraqi engineers by the required expertise and skills. ISE has a number of activities aimed to satisfy their goals by:

1. Establishment of scientific conferences, symposia and events.
2. Establishment continuous education courses and workshops.
3. Organizing scientific publications, lectures and platforms.
4. Supporting scientific studies and researches.
5. Organizing scientific visits.
6. Collecting scientific documents and data bases for engineering purposes.
7. providing expertise and engineering consultancy.

### Administration Commission

- Consultant Engineer Falih Kadhim Zayer\ President of ISE& administration chairman
- Prof. Dr. Hussein Yousif Mahmood\ Vice President of ISE
- Consultant Engineer Ali H. Al-allaq\ Administrative Board of ISE
- Engineer Mohammed Farooq Abdul-khaleq\ Treasurer of ISE
- Asst. Prof. Dr. Maher Yahya Sallom
- Dr. Falih Hamzah Al-Rubyei
- Dr. Hayder Amer Al-Baghdadi
- Lecturer Ahmed Saleh Al-Zuhairi
- Consultant Engineer Riadh Katab Husain
- Consultant Engineer Hamodi Kadeer Mohammed
- Engineer Abdul-lateef H. Sankoor
- Consultant Engineer Abdel Salam A. Issa

## Editorial Board

- Prof. Dr. Hussein Yousif Mahmood\ Editor-in-chief  
University of Baghdad, College of Engineering
- Prof. Dr. Najdet Nashat Abdullah  
Al-Balqa Applied University
- Prof. Dr. Ghada Mousa Rzoki  
University of Baghdad, College of Engineering
- Prof. Maher K. Mahmood Al Azawi  
Al-Mustansiriyah University, College of Engineering
- Prof. Dr. Mohammed Z. Al Faiz  
Alfarhidi University.
- Asst. Prof. Dr. Samira M. Hamdullah  
University of Baghdad, College of Engineering
- Asst. Prof. Dr. Ahmed Zaidan Mohammed Shammari  
University of Baghdad, Al-Khwarizmi College of Engineering
- Asst. Prof. Dr. Naseer A. Al-Haboubi  
Nahrain University, College of Engineering
- Asst. Prof. Dr. Maan Salman Hassan  
University of Technology, Civil Engineering Dept.
- Asst. Prof. Dr. Tawfeeq Wasmi Mohammed  
Al-Mustansiriyah University, College of Engineering
- Lecturer Dr. Ameer Mohammed Rahman Al-Mayah  
University of Baghdad, Al-Khwarizmi College of Engineering
- Lecturer Dr. Basim Abdulrazzak Rasheed  
University of Baghdad, College of Engineering

## Advisors

- Prof. Dr. Ameen Daway Thamir
- Prof. Dr. Majid H. Majeed
- Prof. Dr. Mudaffar S. Al-Zuhairy
- Prof. Dr. Kasim J. Slaiman\ Professor in chemical Engineering
- Prof. Dr. Rami Hikmat Fouad Al-Hadeethi\ Professor in University of Jordan
- Prof. Dr. Ihsan Fethi\ Professor in Architectural Engineering in Denmark
- Prof. Dr. Khalid Al-Sultany\ Professor in Architectural Engineering in USA



## Contents

<b>Design and implementation of Bi-directional power converter for solar energy applications</b> Norhan Mosa Yadgar , Abdulbasit Hasan Ahmed	<b>7-16</b>
<b>Creating a hybrid photovoltaic – diesel generator system for electric generatin</b> Abdulkareem Abdullah Ahmed	<b>17-22</b>
<b>Modeling and simulation for planar biped robot</b> Abbas Hussien Miry , Ali Hussien Mary , Gregor A. Aramice	<b>23-30</b>
<b>Effective adaptive filtering method for salt-and-pepper noise reduction in computed tomography images</b> Abbas Hussien Miry	<b>31-36</b>
<b>On ultrasound elasticity imaging: investigation of correlation window length for breast phantom inclusion differentiation using ultrasound radiofrequency data</b> Ali.R.H. Al-jader , Aws Al-azawi , Taha Ahmed	<b>37-44</b>
<b>Maximum torque per ampere considering different IPMSM drive parameters</b> Farah Mazin Salim , Hanan Mikhael D. Habbi.	<b>45-50</b>

# Design and implementation of Bi-directional power converter for solar energy applications

Norhan Mosa Yadgar<sup>1</sup>, Abdulbasit Hasan Ahmed<sup>2</sup>

<sup>1</sup>Department of Electrical Engineering, North Oil Company

<sup>2</sup> Department of Electrical Engineering, North Oil Company

---

## ABSTRACT

Bidirectional DC-DC converters are widely used in applications that require a bidirectional power flow, like hybrid solar DC-AC inverters, DC-DC battery chargers and electric vehicles (EVs). This research implements an improved solution for hybrid DC-AC inverters, in which the bidirectional converter charges a low voltage (48 V) battery during the normal mode in daylight time (buck converter mode). In the second operating mode, the DC-DC converter will convert the battery voltage to a high voltage (380V inverter bus) in emergency situations (boost converter mode) when the solar panels voltage tends to drop to a certain low level like in cloudy weather or nighttime. The proposed system consists of a phase-shifted IGBT-based full-bridge (FSFB) power stage in the primary side (High voltage side), an amorphous high frequency toroidal transformer that is used for isolation between primary and secondary and for power level shifting between both sides of the converter and a current-fed full-bridge stage on the secondary side (low voltage side). Using the bidirectional converter allows the use of high voltage DC bus for the DC-AC inverter to convert the solar panels DC voltage directly to AC (230Vac) which eliminates the need for a step-up power transformer, which tremendously reduces the system cost and weight. In both directions of power flow of the proposed system, a closed loop control scheme is implemented in software by using a high-performance 32-bit STM32 microcontroller, which is placed on the low voltage side of the system.

---

## KEYWORDS

*Bidirectional DC-DC converter, Pulse width modulation, Buck converter, Boost converter, PID controller*

---

## ARTICLE INFO

Received 9 May 2019

Accepted 20 June 2019

DOI: 10.xxxxx

ISSN: 2413-0230

AL-MUHANDIS Journal (JMISE)

© 2018 Iraqi Society of Engineers (ISE)

E-mail: [jmise@ise-iq.org](mailto:jmise@ise-iq.org)

Online: [www.jmise.ise-iq.org](http://www.jmise.ise-iq.org)

Office Address: Iraq, Baghdad, Al-Nidhal Q.,103-30-5

---

## CORRESPONDING AUTHOR

Name: Norhan Mosa Yadgar

Email:

Research Field:

Google Scholar



## 1. INTRODUCTION

In power systems, where exchange of power is required from the load (DC bus) to the battery and vice versa like home hybrid inverters, energy storage banks or UPS. Where in normal operation, the DC bus is driven from the rectified AC mains of the home or building or from conditioning the voltage of a renewable source of energy like solar panels or wind power generator and the battery can be charged through either the grid voltage or the renewable external source of energy. In a situation where the grid voltage or the renewable energy source is absent, it is required to power the DC bus from the battery to avoid power being interrupted to the load. This is done conventionally with two unidirectional converters, one converter to charge the battery from DC bus (normally, a buck converter) and another converter for converting the battery voltage and feed it to the DC bus (boost converter) in discharging mode. In conventional systems, two power converters are used; each one is processing the power in one direction, which leads to a more cost, space and complexity in the system.

The Bidirectional DC-DC converters are capable of combining two unidirectional converters into single converter allowing bilateral power flow between the battery and the load. The proposed system is an improved design of such a converter that is designed to exchange power from a 48V battery to a 300V to 380V DC bus utilizing full-bridge IGBT power stage on the HV side, which is isolated from a full-bridge MOSFET power stage on the LV side. When the DC bus is present in normal mode, the designed system works in buck mode and charges the battery from the HV DC bus at a constant current until the voltage of the battery reaches the limit. During the absence of the DC bus, the designed system works in the boost mode full-bridge converter to boost the voltage from the 48V battery to the 380V DC bus and backup the load from power outage. During the presence of the DC bus (normal conditions), the design operates in buck mode and charges the battery with constant current until the battery voltage is in regulated limits. During blackouts, the design operates as the current-fed full-bridge converter to boost the power from a 48-V battery (44- to 56-V input) to the 380-V DC bus and supports the load with backup. The change over time from charging mode to backup mode must guarantee the continuity of power delivered to the load. The

transition or change over time from charge mode to backup mode is very critical for ensuring continuity of power to the load. The proposed system has a change over time of about 200  $\mu$ s, which significantly reduces the DC bus capacitors required to maintain an acceptable level of voltage during the change over time. This designed system operates at maximum efficiency of 88% in charger mode (as buck) and 92% as boost (battery discharge mode). Such a higher efficiency in boost mode is achieved thanks to the very low  $R_{ds(on)}$  resistance of MOSFET's used in the LV section which allows more battery run time and less emitted heat. By using an amorphous nanocrystalline transformer core, which has a very high permeability and high saturation induction, leads to much simpler winding procedure and very few number of turns even with lower switching frequencies. Because of using low switching frequency transformer (20 kHz), IGBT's can be used instead of MOSFET's in the HV side which have more robustness and current capabilities than available High voltage MOSFET's. The key specifications of the designed system are listed in Table 1.

Table 1. System key specifications

PARAMETER	TEST CONDITION	MIN	NOM.	MAX	UNIT
<b>BATTERY CHARGER MODE (BUCK)</b>					
<b>INPUT:</b>					
Input bus voltage ( $V_{BUS}$ )	-	300	350	380	V
Input bus current	-	-	-	5	A
Efficiency	$V_{BAT} = 53.4V$ $I_{BAT} = 20A$	-	-	88	%
<b>OUTPUT:</b>					
Output battery voltage ( $V_{BAT}$ )	-	44	48	56	V
Output battery current ( $I_{BAT}$ )	-	-	-	20	A
<b>BACKUP MODE (BOOST)</b>					
<b>INPUT:</b>					
Input battery voltage ( $V_{BAT}$ )	-	44	48	56	V
Input battery current ( $I_{BAT\_MAX}$ )	$V_{BAT} = 53.4V$	-	-	50	A
Efficiency	$V_{BAT} = 53.4V$ $I_{BAT} = 50A$	-	-	92	%
<b>OUTPUT:</b>					
Output bus voltage ( $V_{BUS}$ )	$V_{BAT} = 53.4V$	300	350	380	V
Output bus current		-	-	7	A



## 2. HARDWARE IMPLEMENTATION

### 2.1 HIGH VOLTAGE (HV) POWER STAGE

The first power stage of the designed system (HV stage) is consisted of an IGBT based full-bridge to act as a step down converter in charging mode (buck) and works as full bridge rectifier in boost mode. The purpose of this stage is to step down the 400V DC bus voltage in combination with a high frequency amorphous transformer, which gives a galvanic isolation between primary and secondary.

The primary side (HV stage) full bridge is driven with phase shift modulation technique, which is used to obtain Zero Voltage Switching (ZVS) to minimize the turn-on switching losses of the primary switches, unlike the traditional PWM that operates the transistors in hard switching mode, and significant amount of power is lost. Therefore, the phase shifted full bridge is more suitable for high frequency and power applications.

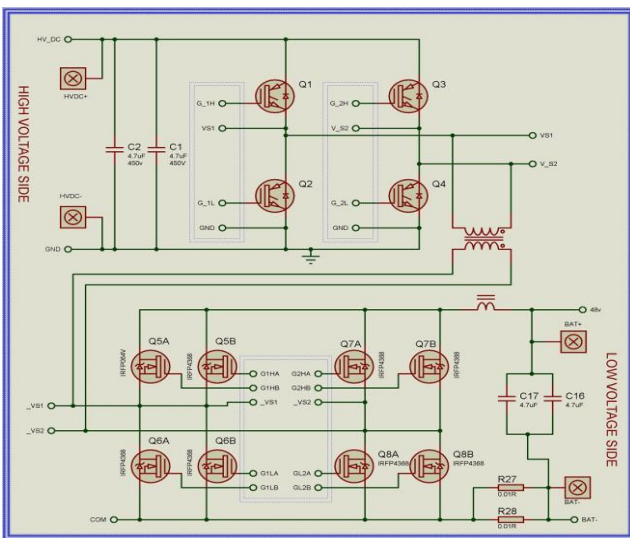


Figure 1. Power stage schematic of the designed system

Each leg of the primary side (HV) converter (Q1&Q2, Q3&Q4) is driven by two complementary PWM signals at a fixed 50% duty cycle. The implementation of phase-shifted modulation is done by delaying the two complementary square waves of the second leg (Q3 and Q4) with respect to the reference square wave of the first leg (Q1 and Q2) as explained in Figure 2. A dead time of 1µs is inserted

between the high and low side driving signals for each leg of the primary full bridge which is necessary to avoid cross conduction between Q1-Q2 and Q3-Q4. The modulation is implemented by delaying in phase the two square waves of the lagging-leg (Q3 and Q4) with respect to those of the leading-leg (Q1 and Q2), as shown in Figure 2.

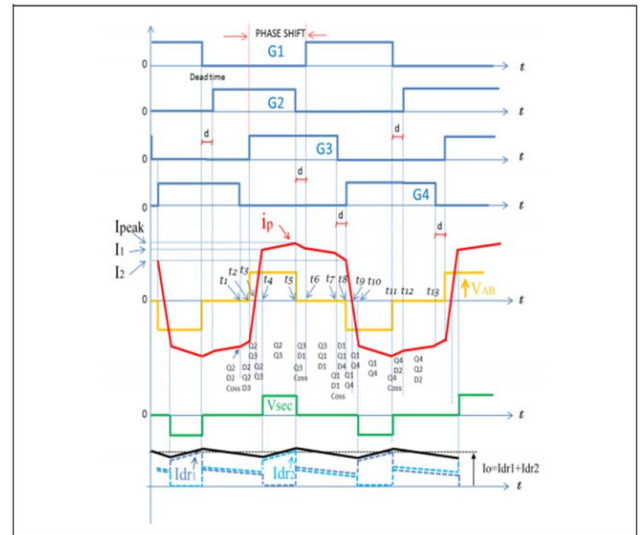


Figure 2. Gate signals, transformer primary current and voltage of the of the bidirectional converter

The phase shift angle between the two legs of the bridge determines the duty cycle of the bipolar voltage applied to the primary or the induced voltage on the secondary of the transformer (the green waveform in Figure 2). Thus, the controller is responsible for adjusting this phase angle according to the required battery voltage when used as charger and is explained in the Microcontroller board section.

### 2.2 HIGH FREQUENCY TRANSFORMER CALCULATION

By using an amorphous nanocrystalline high-frequency transformer, which has a very high permeability and high saturation induction. This enables much simpler winding procedure because the traditional ferrite based cores require very high number of turns (typically 300 turns) compared to the amorphous Fe-based Nanocrystalline core, which requires 22 turns at 400V Vbus (according to the core datasheet) only in the primary side at the same frequency.

The transformer turns ratio for the designed system can be calculated using the formula:

$$\frac{N_{pri}}{N_{sec}} = \frac{V_{in\_min}}{V_{out\_max}} * \delta_{max} \quad (1)$$

Where  $N_{sec}$  is the secondary turns number,  $N_{pri}$  is the primary turns number and  $\delta_{max}$  is the maximum duty cycle appearing at the transformer secondary winding at one switching period. In designed system, the maximum duty cycle is estimated as  $\delta_{max} = 0.8$  and taking into consideration of the duty cycle loss, dead-time of the driving signals and maximum phase shift determined by control loop and can be calculated as:

$$\begin{aligned} N_{pri} / N_{sec} &= V_{in\_min} / V_{out\_max} \\ &= 300 / 56 * 0.8 \approx 4.3:1 \end{aligned}$$

The selected transformer core is T56\*28\*28 which is, according to the manufacturer, is capable of delivering between two to three kilowatts. The transformer's primary (HV side) must be designed to withstand the maximum bus voltage, According to the manufacturer's datasheet, the number of turns for the primary side at 30kHz switching frequency and 400V input voltage is equal to 22 turns, therefore, the secondary turns is equal to  $22 / 4.3 = 5.1$  Turns. Rounding to the nearest integer, the number of turns is equal to 5 turns. Two groups of the secondary windings were added in parallel and distributed regularly around the core to increase the mutual inductance between the primary and secondary as shown in Figure 3.

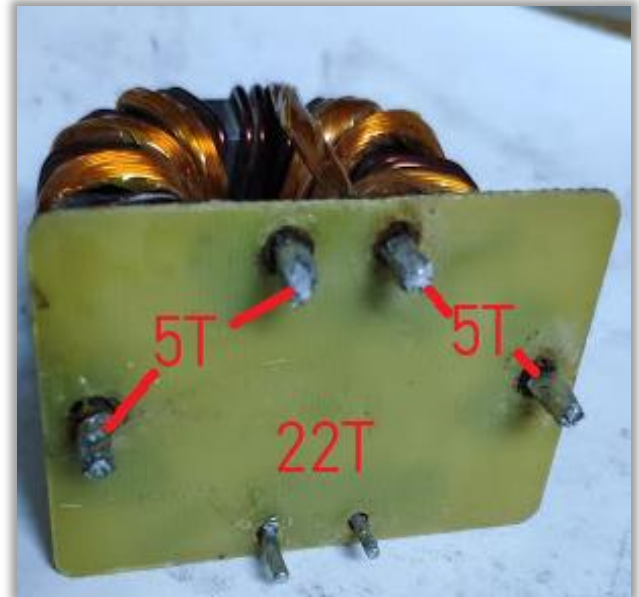


Figure 3.b The final form of the transformer

### 2.3 LOW VOLTAGE (LV) POWER STAGE.

The output power stage (LV stage) of the designed system consists of MOSFET based full bridge. Each leg of the bridge consists of two MOSFET's in parallel to increase the current capabilities of the converter and to increase the overall efficiency of the system by reducing the amount of heat generated by the low voltage side switches due to the higher flowing current. In backup mode (boost mode), the designed system boosts the battery voltage that is between 44 to 56 V to a 350 V DC output. The topology suited for this purpose is either a voltage-fed or current-fed converter. The voltage-fed have the input capacitors connected across the power stage and an output inductor. The voltage-fed topology have several advantages over the current-fed converter like the boosted input voltage that reduces the stress on the transformer, avoiding imbalance of the flux that is presented in the current fed converter's power stage and lower the stress on the input capacitors because of the inductor. However, the voltage-fed converter is not suited for the charger mode because the filter capacitors are connected directly after the full-bridge of low voltage side (before inductor) as shown in Figure 3. By the varying in phase shift of the input (varying the phase shift in the HV side produces a variable duty cycle on the LV side as described in the previous section ) does not alter the voltage on the



Figure 3.a The final form of the transformer

output because of the output filter capacitors (C16 and C17 in Figure 3a.) are being rapidly charge during the on time. During the off time, the output filter capacitors conserve a considerable amount of charge, especially with light load connected, therefore; the output voltage is still at same level or slightly changed even when varying the phase-shifted angle between 0 and 180 degrees. The varying output voltage is essential with buck mode (charger) so, the voltage-fed topology is not suitable for the designed system despite its several advantages in boost mode.

(LV) have an extremely low on-resistance and thus, the conduction losses are very low compared to diodes rectifier. The low voltage side of the designed system have each Mosfet doubled in order to increase current capability as mentioned before, IRFP4468 (100V, 2 mΩ and 195 A max current) MOSFET have been selected due to its extremely low resistance and having very high current ability making it a good solution for such a converter. In Figure 1, each diagonally positioned transistors in the low voltage side (Q5A, Q5B, Q8A and Q8B) are turned on and off at the same time with the primary transistor Q1. Similarly, the other diagonal transistors (Q6A, Q6B, Q7A and Q8B) are also synchronized in gate drive signals with the HV transistor Q2 which means that the MOSFET's of output stage are always synchronized with first leg of the high voltage side (Q1 and Q2), figure 4. shows an example of 90° phase shift angle between the first leg (Q1 and Q2) and the second HV leg (Q3 and Q4).

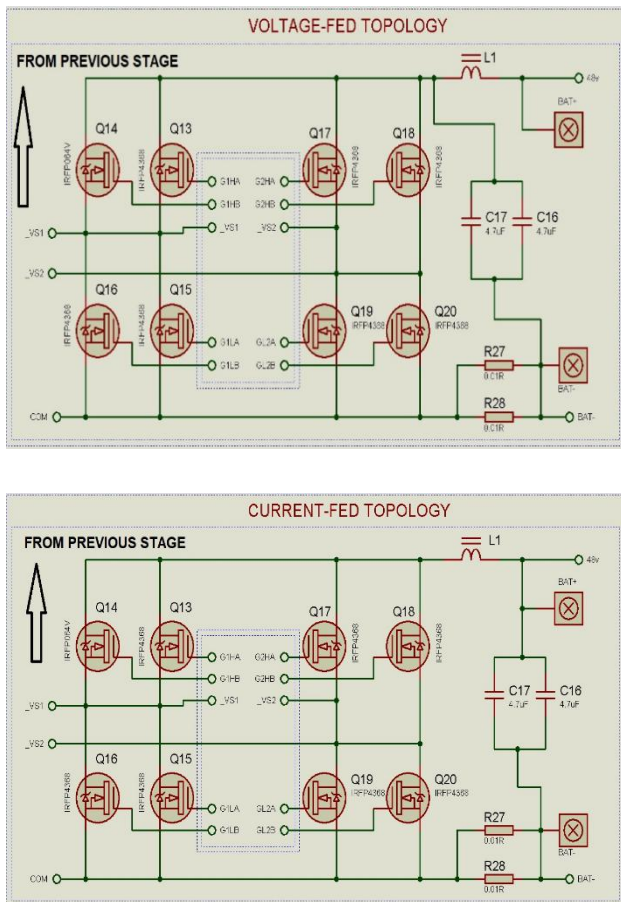


Figure 3. (c): Voltage-fed converter.  
 (d): Current-fed converter.

The designed system is chosen to be a current-fed converter in boost mode and also works as a voltage-fed buck converter when working in charger mode. In charger mode, the converter transfers the power from the primary (HV side) DC bus and charges the 48V battery pack (four 12V/150AH, gel type solid-acid, deep-cycle batteries in series) in constant current/constant voltage (CC/CV) mode. The charging current is limited by software to 20 A. The low voltage (LV) side in charging mode works as a synchronous rectifier to enhance the efficiency of the system as the MOSFET's used in the secondary side

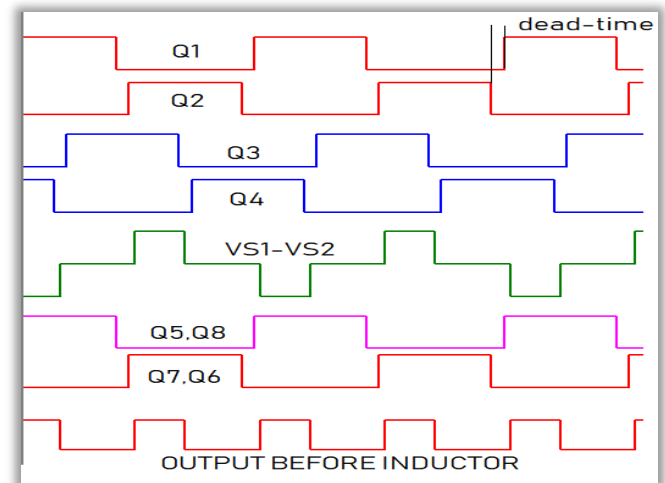


Figure 4. Example waveforms for all transistors (HV and LV) in charger mode with 90° phase shift

In boost mode, the high voltage side transistors are turned off because synchronous rectification does not give any benefits when using IGBT's because the turn on voltage of the IGBT ( $V_{CE}$ ) is larger than its internal freewheeling diode's forward voltage (about 2.5 V saturation voltage for IGBT vs 1V forward voltage for diode). Therefore, if the high voltage IGBT's are turned off in boost mode, the built-in four diodes in each IGBT will form a full-bridge diode rectifier to rectify the alternating voltage from the transformer and smoothed by the HV side filter capacitors to power the DC bus.

## 2.4 CURRENT-FED INDUCTOR DESIGN

The maximum voltage of the input battery when fully charged  $V_{BAT\_MAX} = 56$  V. The maximum appearing voltage across the transformer's primary winding must be chosen to be higher than this voltage in order for the current-fed power stage to maintain the boost action. To achieve a minimum boost ratio, the voltage on the low voltage side ( $V_{PRI}$ ) when the HV DC bus is 380 V is given in Equation 2:

$$V_{PRI} = 1.1 \times V_{BAT\_MAX} = 61.6 \text{ V} \quad (2)$$

By selecting the  $V_{PRI} = 61.6$  V, a sufficient voltage margin can be maintained on the 100-V MOSFET's in the low side (IRFP4468) taking into consideration the voltage spikes at turnoff (dead-time) caused by the current-fed inductor. A relatively low switching frequency is selected (30 kHz) accounting for the best operating frequency range for the amorphous transformer and IGBT's. This will help minimizing the switching losses of the switches in both sides of the converter and maintain a high efficiency. Assuming an efficiency of 90%, the maximum battery input power  $P_{IN\_MAX}$  is given in Equation 3:

$$P_{IN\_MAX} = \frac{P_{OUT\_MAX}}{\text{Efficiency}} = \frac{2000}{0.9} = 2222.2 \text{ W} \quad (3)$$

The minimum usable voltage for the 48 V battery pack is set to 44 V to avoid the batteries being completely drained, the maximum average input current  $I_{IN\_MAX}$  will be:

$$I_{IN\_MAX} = \frac{P_{IN\_MAX}}{V_{BAT\_MIN}} = \frac{2222.2 \text{ W}}{44 \text{ V}} = 50.5 \text{ A} \quad (4)$$

The inductor ( $L_1$ ) calculation procedure is similar to the one used for boost converter, the maximum allowed inductor ripple percentage ( $I_{IN\_MAX\_RIPPLE}$ ) and the maximum period of which all the MOSFET's full-bridge in the LV side are on simultaneously ( $V_{PRI}$ ). In order to find  $D_{MAX\_OVERLAP}$ ,  $D_{MAX}$  need to be calculated by Equation 5:

$$V_{PRI} = \frac{V_{BAT\_MIN}}{2(1-D_{MAX})} \quad (5)$$

This yields:

$$D_{MAX} = 1 - \frac{V_{BAT\_MIN}}{2V_{PRI}} = 0.643$$

$D_{MAX\_OVERLAP}$  can be calculated from Equation 6:

$$D_{MAX\_OVERLAP} = D_{MAX} - 0.5 = 0.143 \quad (6)$$

By setting the inductor ripple to 40% , the  $I_{IN\_MAX\_RIPPLE}$  can be found from Equation 7:

$$I_{IN\_MAX\_RIPPLE} = I_{IN\_MAX} \times 0.4 = 20.2 \text{ A} \quad (7)$$

Finally,  $L_1$  can be calculated from Equation 8:

$$L_1 = \frac{V_{BAT\_MIN} \times D_{MAX\_OVERLAP}}{I_{MAX\_RIPPLE} \times F_{SW}} = 10.4 \mu\text{H} \quad (8)$$

In order to wind this inductor, the peak inductor current  $I_{IN\_PEAK}$  needs to be calculated by Equation9:

$$I_{IN\_PEAK} = I_{IN\_MAX} + \frac{I_{IN\_MAX\_RIPPLE}}{2} = 60.6 \text{ A} \quad (9)$$

The inductor of the current-fed converter should have a toroidal core with material that have a low loss, relatively high saturation level and capable of operating at high frequencies. We chose the very popular material ideally suited for this type of applications known as "Kool Mu" material. The part number of the toroidal core we used is the Micrometals Arnold's MS-157060-2 with a permeability of 60 and a nominal AL value of 81 nH/N<sup>2</sup>.

In order to get a 10.4  $\mu\text{H}$  from this core, we must ensure that the DC magnetizing force (H) is less than the limit of this core. The first thing we do is determining the number of turns required to get the required inductance at  $I_{IN\_PEAK}$  (60.6A). Firstly, we calculate the DC Energy Storage in the inductor:

$$J = \frac{1}{2} L \times I^2 = 19096 \mu\text{J} \quad (10)$$

From the DC Energy Storage vs. NI (ampere-turns) curve in the datasheet as shown in Figure 5, we find that the NI product is about 1200 ampere-turns.

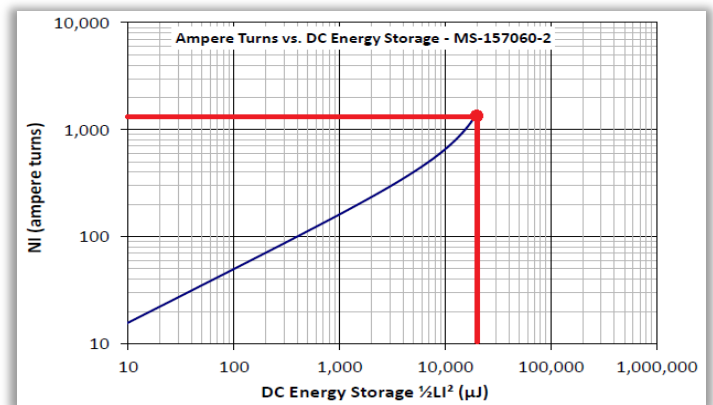


Figure 5. DC Energy Storage vs. NI (ampere turns) curve for the core

Again, from the AL Value (nH/N<sup>2</sup>) vs the NI (ampere turns) table found in the core datasheet, the



AL value at the given load current drops to 25 nH/N<sup>2</sup>,

Therefore, the required number of turns is equal to:

$$N = \frac{N \times I}{I} = \frac{1200}{60.6} \approx 20 \text{ Turns} \quad (11)$$

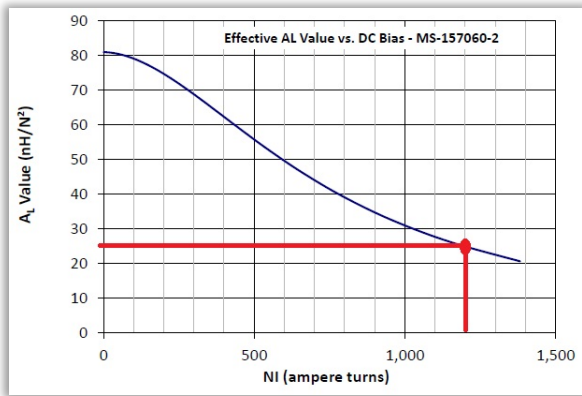


Figure 6. AL Value (nH/N<sup>2</sup>) vs the NI curve for the core

## 2.5 GATE DRIVERS IMPLEMENTATION

Because of using phase shifted full bridge topology in the high voltage, the duty cycle of each leg is constant at approximately 50%. Therefore, using a transformer with one primary and two separate, identical, 180° out of phase and isolated secondary windings, having turns ratio of 1:1:1 for driving each leg is an ideal solution as shown in figure 7.

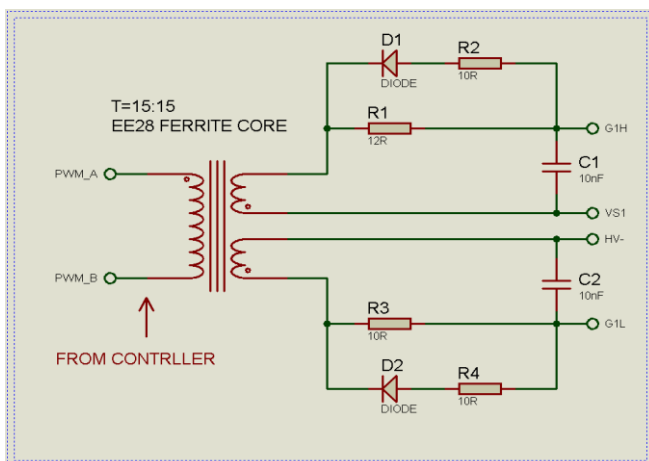


Figure 7. Transformer gate driver for each leg of the HV side transistors

This method of driving will have many advantages over the photo-isolated gate drivers include:

- Cross-conduction prevention is guaranteed between the upper and lower transistors no matter what happened in the primary section.

- Photo-isolated drivers require isolated power supply for each transistors, which adds more system cost, size and complexity.
- Transformer based gate drivers are more rigid and robust than electronic-based drivers.
- The ability to change the ratio of the gate driver pulse transformer adds more system flexibility in case of using a power supply with a voltage below or higher than the drive signal requirements. For example, when using 5 V power supply for the system, the IGBT requires ±15 V for the gate to be turned on or off. Therefore, the primary windings of the gate driver transformer can be wound less than the number of turns of the secondary or 1:3:3 to achieve the IGBT gate driver requirements.

The primary windings of the gate transformer is supplied with bipolar PWM signals from the microcontroller (via a push-pull transistors stage to boost the current capability). Let us take the upper part of Figure 7. Understand how transistors are driven. When a negative pulse applied to the primary, the current will flow through R1 to the IGBT gate, C1 help slow turning on of IGBT to avoid high di/dt ratio of the transistor, which could destroys it in high loads. Transistor will remain on the entire duration of the pulse. Meanwhile, the lower transistor is turned off because negative voltage has been applied to its gate because of the reversed polarity of its gate drive windings. When positive pulse is applied to the primary, D1 will conduct and R2 becomes in parallel with R1, turning the on IGBT faster than off. This will ensure the counter transistor to turn on after the other is turned on to ensure there is a dead time between each driver signal. In the low side (LV), the principle of driving is similar to the HV side but MOSFET's requires less gate voltage to be turned on. A 10 V is enough for the MOSFET to be properly turned on so the gate driver transformer need to be designed to boost the 5 V signal from controller to 10 V. So, the turns ratio of the LV side gate driver transformer is wound in a 1:2:2:2 ratio with one primary winding and four secondary windings to drive all the MOSFET's in the LV side.

Figure 8. shows the gate driver transformers for the HV side (right) and LV side (right).

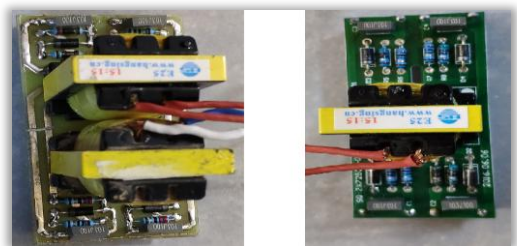


Figure 8. Gate driver transformers: (left) HV side, (right) LV side.



## 2.6 POWER CIRCUIT DESIGN

The power circuit is as mentioned in the previous sections contains two full-bridge transistors in low and high side, power transformer, input/output filter capacitors and inductor in the low voltage side. All these components are put in one single printed circuit board improve the thermal stability of the system and must be well-placed and laid out to avoid unwanted circulating current loops and noise. The printed circuit board (PCB) is designed using Proteus design software with double layer board to shrink the board size as possible. Figure 8. shows the PCB of the power stage:

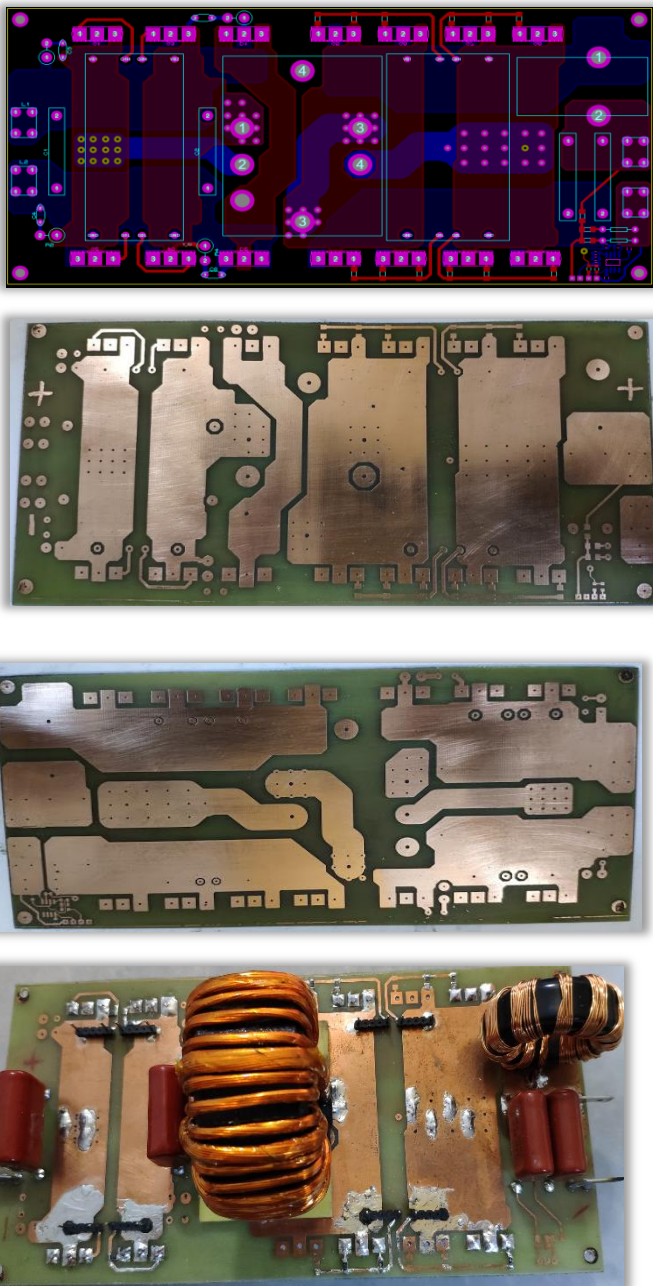


Figure 8. From top to bottom (1): Designed PCB in Proteus. (2): Top side of the PCB. (3): Bottom side of the PCB. (4) The assembled final board.

## 3. CONTROL SIDE IMPLEMENTATION

### 3.1 Microcontroller part

The selected Microcontroller is the STM32F030K6T6 from ST microelectronics, which embeds a 32-bit Cortex-M0 core running at 48 MHz frequency with 32 kBytes flash and 4 kBytes of RAM with extensive set of peripherals such as a 12-bit, 1.0  $\mu$ s ADC (Analog to Digital Converter), Nine 16-bit general purpose timers, One 16-bit timer with six-channels PWM, dead-time generation and emergency stop used to generate the PWM signals to drive the DC-DC converter, 5-channel DMA controller and many other advanced peripherals. The microcontroller is the brain of the whole design, it monitors the voltage/current of input/output stages, select the mode of operation (buck/boost) and drive the high and low side transistors. Figure 9. Shows the microcontroller prototype board designed and printed in the same way as power board.

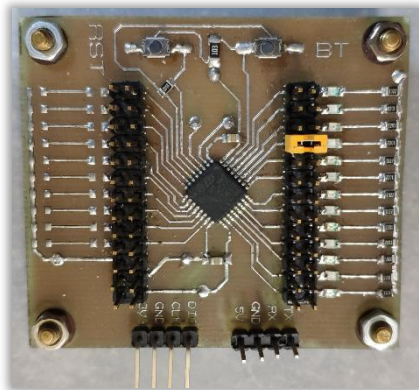


Figure 9. Microcontroller finished board

### 3.2 Software Implementation

We used CoIDE, a free integrated development environment focusing on ARM Cortex-M0 /M0+/M3/M4 based microcontrollers. It uses GCC (GCC-ARM-Embedded) tool chain that is based on Eclipse integrated development environment (IDE).

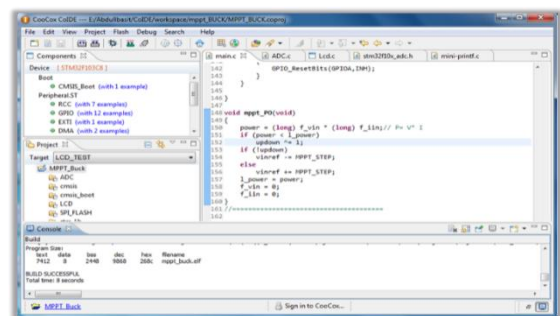


Figure 10. The CoIDE Integrated development environment

The control of battery charging is implemented in software such that the microcontroller continuously monitors and adjust the charging voltage/current until the battery is fully charged. There are two main control loops, the first one is for controlling the output voltage/current of the low side (LV) when used as a charger and running at 50 kHz, the other loop is for adjusting the output boosted voltage of the high side when the converter is running in backup mode (boost) running at 10 kHz. The over voltage and over current for both power stages (HV and LV) are interrupt driven so that the system acts as fast as possible for the given event and disables all PWM signals until the event clears. The background loop is used for non time-critical operations such as serial communications for settings and displaying the readings to the terminal program running at the computer side.

#### 4. EXPERIMENTAL RESULTS

After finishing the PCB design and printing all the boards in toner transfer method, the system components have been assembled, programmed and tested.

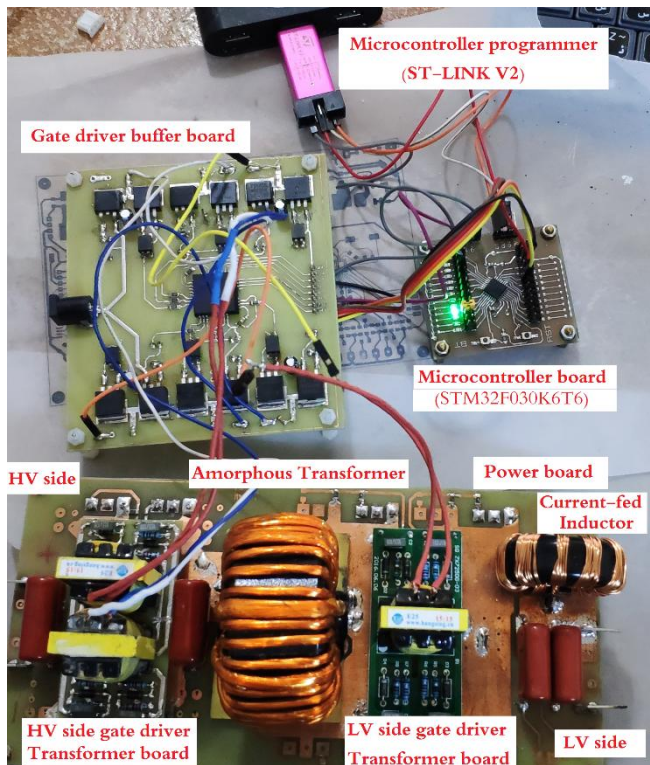


Figure 11. The final assembled system components.

After completing the circuit design, transformed the schematic to PCB using Proteus software, building the circuit and programming the microcontroller, the system maximum power has been in buck mode tested using a heater resistor. The input voltage was 320 VDC rectified from AC mains of 230 VAC the output

voltage is set to a fixed value (49 V) in software in order to get full rated power (the CC/CV charging algorithm was disabled in test mode because it does not allow more than 20 A output) . After connecting the resistive load to the low voltage side, the voltage was fixed to the set point (49 V) and a full rated current is drawn with efficiency of 92% at full load.



Figure 12. The final assembled system components.

The final experimental setup is shown in figure 12. The maximum efficiency is obtained at full power (2 kW) as shown in Figure 13:

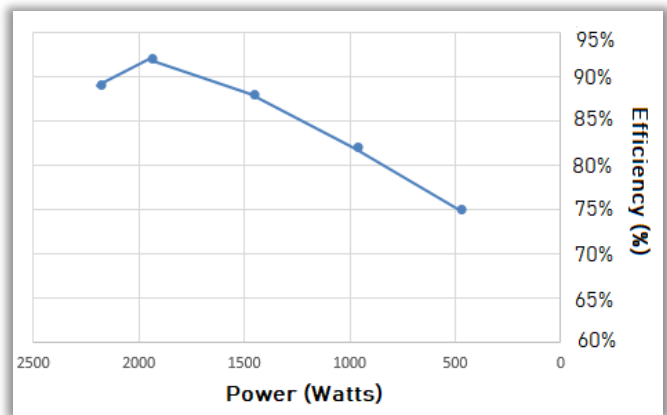


Figure 13. system efficiency vs. output power in buck mode.

#### 5. CONCLUSION

This work has been focused on improved design and implementation details of microcontroller-based isolated bidirectional converter that is rated for 2 kW of output power in either direction. The HVDC bus is ranged from 300 V to 380 V, while the secondary low voltage is ranged from 44V to 56V to charge a 48 V battery pack. The design showed that using a modern transformer high frequency material (amorphous Fe-based nanocrystalline) instead of ferrite can highly improve the design in terms of increased output power and power density (4 kW/liter). The very high



permeability and high saturation induction of the transformer core allows much less transformer turns as compared to the traditional ferrite-based cores and hence, less copper is needed for windings which leads to less transformer losses, higher system efficiency and reduced system cost and weight. The transformer material is best suited for frequencies from 10 kHz to 50 kHz which, which means that using IGBT's instead of using MOSFET's in former high frequency materials to achieve higher power is possible. By combining the amorphous cores with IGBT's, much larger power converters could be easily implemented of up to tens of kilowatts because the IGBT's are readily available in ratings of hundreds of amperes. This work is primarily designed for solar energy applications and to be used with an inverter that is connected in parallel with converter's HV side. Both of inverter and the bidirectional converter are powered from HV DC bus from solar panels. This means that the inverter is always fed with high voltage either from solar panels or from the designed converter, allowing it to directly convert the HV dc voltage to a usable AC voltage without the need for a step-up transformer as used in traditional commercial inverters and also eliminates the need for a separately sold charge controller which considerably reduces the system cost, weight and complexity.

## 6. REFERENCES

- [1] IEEE, Operation principles of bi-directional full-bridge DC/DC converter with unified soft-switching scheme and soft-starting capability, 15th Annual IEEE Applied Power Electronics Conference and Exposition, 2000.
- [2] IEEE, Extended Range ZVS Active-Clamped Current-Fed Full-Bridge Isolated DC/DC Converter for Fuel Cell Applications: Analysis, Design, and Experimental Results, IEEE Transactions on Industrial Electronics (Volume: 60, Issue: 7, July 2013).
- [3] Texas Instruments, Bidirectional DC-DC Converter, TIDM-BIDIR-400-12 Design Guide (TIDUAI7).
- [4] IEEE, Isolated full bridge boost DC-DC converter designed for bidirectional operation of fuel cells/electrolyzer cells in grid-tie applications, 15th European Conference on Power Electronics and Applications (EPE), 2013.



# Creating a hybrid photovoltaic – diesel generator system for electric generating

Abdulkareem Abdullah Ahmed

Renewable Energy & Environment research Center/ Corporation of Research and Industrial Development/ Baghdad – Iraq

---

## ABSTRACT

Many applications which are sensitive need to be provided continuously by electrical power, like laboratory equipment, far away zones that not provided with local electrical grid, and military boundary points. It is modeled a hybrid system containing photovoltaic – battery system with diesel generator. The modeling considered the PV system as main source to provide electric power and the diesel generator an auxiliary source working in emergency cases. The research aims to build a reliable hybrid system to provide electrical power, it is noticed that the reliability is proportional with system components numbers. The system performance reliability depends on basic items as system parts maintenance and their quality which depends on the technique used in manufacturing these parts that is affect the system operation continuously, and operation cost.

---

## KEYWORDS

Hybrid photovoltaic, diesel generator, electrical power, grid, operation.

---

## NOMENCLATURES

ATS	Auto transfer switch
1-R <sub>SS</sub>	probability of (ATS) operation continuously failure
P <sub>s</sub>	Probability of (ATS) switching success
Q	Unreliability
Q <sub>s</sub>	Probability of (ATS) switching failure
R	Reliability
R <sub>p</sub>	Reliability of parallel system
R <sub>s</sub>	Reliability) of series system

---

## ARTICLE INFO

Received 9 May 2019

Accepted 20 June 2019

DOI: 10.xxxxx

ISSN: 2413-0230

AL-MUHANDIS Journal (JMISE)

© 2018 Iraqi Society of Engineers (ISE)

E-mail: [jmise@ise-iq.org](mailto:jmise@ise-iq.org)

Online: [www.jmise.ise-iq.org](http://www.jmise.ise-iq.org)

Office Address: Iraq, Baghdad, Al-Nidhal Q.,103-30-5

---

## CORRESPONDING AUTHOR

Name: Abdulkareem Abdullah Ahmed

Email:

Research Field:

Google Scholar:

## 1. TYPES OF SYSTEM CONNECTION [2]

### 1. Two System Parallel Connection:

A system with two independent units (A) and (B) are connecting as in Figure (1), and the probability of success or reliability (R) related with the probability of failure or unreliability (Q) for each unit.

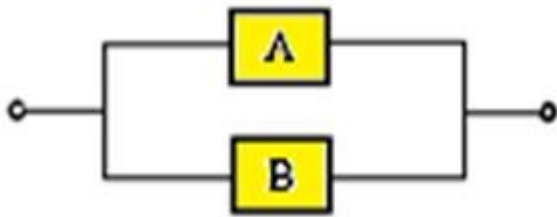


Fig (1) Parallel Connection System

The probability of an event of two events one of which is complementary to the other, and each event has a proportion of incidence so that their sum equals one.

$$R_A + Q_A = 1 \quad (1)$$

$$R_B + Q_B = 1 \quad (2)$$

Where:

The reliability of Parallel system ( $R_P$ ) is

$$R_P = 1 - Q_A \cdot Q_B \quad (3)$$

$$R_P = R_A + R_B - R_A \cdot R_B$$

### 2. Two System Series Connection:

The Reliability of series system ( $R_S$ )

$$R_S = R_A \cdot R_B \quad (4)$$

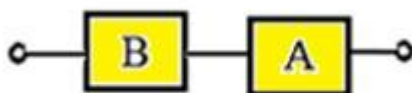


Fig (2) series Connection System

### 3. Parallel-series Systems:

It is important to operate one of the parallel units in the system as main and the other works in case emergency, this needs to be controlled through a Sensing Subsystem under a certain mechanism of connection, using a secondary connection system as shown in the following diagram, Figure (3).

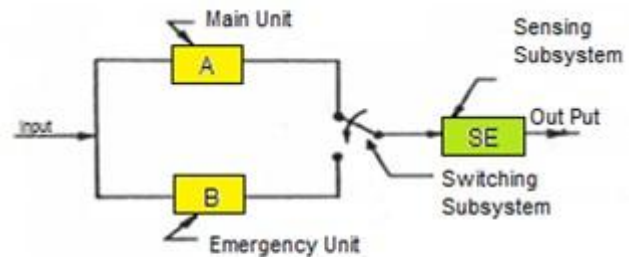


Fig (3) Main Unit, Emergency Unit, Sensing subsystem Connection

The reliability of this system is one of three cases:

1. The unit (A) succeed to work for the time of the task period (T), and the sensing system will not work and then no failure of the system.
2. The unit (A) fails to complete the task before the specified time period (T), and the sensor system works at time ( $t_1 < T$ ), The self-switching unit is then works to connect unit (B) and then the main unit separated, the system continues to achieve function until the task is completed over time (T).
3. When the task in item (2) take place and the sensing system and the self-switching unit working to reconnect the unit then unit (A) works at time ( $t_2$ ). The chronology is ( $t_1 < t_2 < T$ ). There are two possible failures, first, switch does not work then unit (A) does not work and unit(B) continue working. Second, sensing unit works and connecting main unit (A) to perform the task and separate unit (B).

The probability of the switching success is symbolized ( $P_s$ ) and the probability of failure symbolizes ( $1 - P_s$ ), therefore the probability of failure of the system

$$Q = Q_A - Q_A P_s (1 - Q_B) \quad (5)$$

The value of ( $Q_B$ ) is affected by the time factor required to operate the unit (B). The probability of switch fault after an operation period and switching to unit (B) is very rare. The probability of its operation is symbolized ( $R_s$ ) and its probability of failure ( $Q_s$ ).

The system with the self-switching unit is represented as in figure (4).

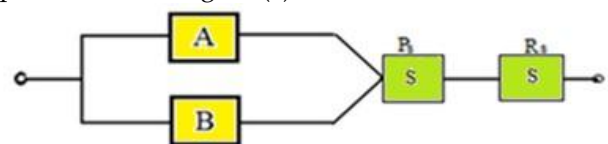


Fig (4)  
System circuit representation

There are two components representing self-switching unit, one is ( $P_s$ ) as exchange mode and the second represents normal mode of operation



considering its reliability (Rs) and failure status (Qs) and are correlated with one of the two parallel units (A and B) and the reliability of the system is as follows

$$R = R_s(1 - (Q_A - Q_{APs}(1 - Q_B))) \quad (6)$$

### 1. FAILURE RATE [3][4]

The number of times the failures occurrence in a particular system, or any unit in the system during a specific period of time. The failure rate of any system depends on the factor of time where the number of failures of any system during its first operation (new system) is usually lower in the advanced periods (old system) of its operation.

$$Q = \frac{\text{Number of failures}}{\text{Task life time}} \quad (7)$$

### 2. RELIABILITY REQUIREMENTS

One of the reliability important priorities of any system is allocating reliability requirements and adequate maintenance, which can be achieved by appropriate analysis of the faults that occur or the results of the test. In addition to the adoption of high quality products whose origins are certified with high reliable in performance.

Photovoltaic systems are highly reliable systems with low faults if the rated values of their components are calculated accurately and in proportion to the nature of loads, depending on the climate situation in that region and the weather conditions surrounding the system, The reliability in this case is affected by the frequency of this failure, and the time period required by the system for task completion, in a few cases occur, such as increasing the number of times blocking the sun because of clouds and dust cases more than the number taken into account in calculating the values of components, the possibility of failure in The work of the system is very likely [5].

For diesel electric generator and other system components, the reliability is high at operating early life, and decreases at their advance of life. [6]

### 3. EXPERIMENTAL PART

The practical part requires the following requirements

Photovoltaic System

Number of modules is (20) modules each of maximum power (250) watt to provide power of average (640) watt along (24) hour a day.

(16) Gel Battery with capacity 0f (200) Ah.

Inverter has characteristics (Rated power (1.3 kW), DC Side Voltage (48V), AC Side Voltage (220V), Rated Current (6 A).

Charging Controller of charging voltage (48) volt and charging current (75) A.

Diesel-Electric Generator is works when emergencies occur in the photovoltaic system Such as low battery voltage due to discharge and insufficient solar power falling on PV panels due to solar radiation being blocked by clouds or anything else. The generator is highly reliable to ensure operation in emergency situations. Single phase, Load Rating (5kW), Rated voltage (220V ±5%), Frequency range (50Hz±1%)

### Auto Transfer Switch(ATS) [7]

The Auto transfer-switch switches the generator to provide power to the loads when the photovoltaic power fails to process, it sends an instruction to start operating the generator. Generator operation takes multi steps, first, heating the nozzles, starting the engine self-starter, then connecting the load to the generator.

When the photovoltaic restart operating, the (ATS) switch the power to the load from generator to the PV system, then stop generator operation after a time for cooling the generator, this time can be controlled by the delay timer as shown in fig (5).

Low, High Voltage Sensor

This device sense the low and high voltages provided to the inverter in the discharge state and in the charging state. It detects the voltage drop at (11.5V) and activates the auto transfer switch for its function. The sensor also works when the battery voltage rises to (12.75 V) after the charging completion to stop generator and re-providing power from the PV system.

Loads

The load is inductive and resistive of (1kW) loading the hybrid system through contactor switch. The electrical circuit diagram is as in fig (5).

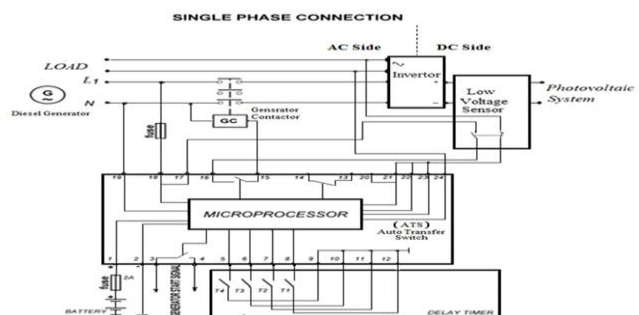


Fig (5). Circuit Diagram of Auto Transfer Switch, Voltage Sensor, Inverter



#### 4. WORK PROCEDURE

The equipment used in the research are connected to each other under the circuit in fig (5). Where the following procedures were taken experimentally to simulate the system that the weather is cloudy and for one day was as follows:

The load is provided with electrical energy from the photovoltaic system. The system worked normally. The output voltage of the inverter was (227) volts and the input voltage was (51.5) volts.

Open the electric circuit that feeding the inverter from the PV system to let battery voltage be reduces, or open the battery circuit in order to make voltage sensing unit operate, it operates at (46.1) volt.

Record the time taken by the voltages sensor to energize the (ATS), it was (5) seconds.

Record the time taken by the (ATS) to operate the generator and energize the main contactor to provide electricity to the load.

After the charging is complete and continue providing electrical power to the loads, when the battery voltage becomes (51.5) volts, the charging current shall be as low as possible. This will cause the voltage sensor to detect high voltages and lead the (ATS) to disconnect the load from the generator and equip it with the photovoltaic system. The generator motor continues working to complete the cooling process for (30) seconds to turn off the generator.

This process was repeated five times and the previous readings were very close, as in Table (1).

#### 5. HYBRID SYSTEM FAULTS:

- 1) Photovoltaic System: Occurs cloudy or dusty days (5) times during (30) days throughout the year.
- 2) Diesel-Electric Generator: As the generator is new, potential faults are limited during the first year and more complex faults occur during the second year, and then the approved and necessary maintenance Procedures reviewed from the operation and maintenance manual, taking into account actual hours of operation, as follows;
  - a. Changing the oil filter once a month.
  - b. Changing the fuel filter once every two months.
  - c. Changing the air filter once every 6 months.
  - d. Maintenance of the generator engine once every two years.
  - e. Failure to operate the generator for atypical reasons once every 6 months as a result of leakage of air into the fuel system, or the adoption of bad fuel.

- 3) Auto Transfer Switch (ATS): There are two possibilities for the failure to occur, the first, the switch do not achieve the connection, with the reliability of the system symbol is (PS) and the state of failure (1-PS). The second failure is during the connection, and the operation of the switching system and the operation of the system (power generator), this is rare and the reliability of the system symbol (RSS) and the failure is (QS). It is represented by series connection. The probability of occurrence of the first case is every two years, and the possibility of occurrence of the second case every three years.

#### 6. RESULTS AND CALCULATIONS

The results are recorded, and the hybrid system reliability is calculated, see table (1).

Table (1).

The test readings and the operation timing of the (ATS)

Table (1)

Test readings and the operation timing of the (ATS)

	Inverter		
	DC Side Volt		AC Side Volt
	From	To	
Discharging	51.5	46.1	22V
Charging	46.1	51.5	22 <sup>a</sup>
Low voltage sensor	On Time of (ATS + Generator Operation + Contactor)		Change over time
5(sec)	40(sec)		45(sec)

#### 7. THE CALCULATIONS:

Using Formula (7)

- 1) More than one cloudy or dusty days' probability ( $Q_A$ ) and reliability ( $R_A$ )
 
$$Q_A = 5/30 = 0.167$$

$$R_A = 1 - Q_A$$

$$= 1 - 0.167 = 0.833$$
- 2) The probability of oil filter changing ( $Q_{B1}$ ) and the reliability ( $R_{B1}$ )
 
$$Q_{B1} = 1/30 = 0.033$$

$$R_{B1} = 1 - Q_{B1}$$

$$= 1 - 0.033 = 0.967$$



- 3) The probability of fuel filter changing (QB2) and the reliability (RB2)  
 $Q_{B2} = 1/60 = 0.017$   
 $R_{B2} = 1 - Q_{B2}$   
 $= 1 - 0.017 = 0.983$
- 4) The probability of air filter changing (QB3) and the reliability (RB3)  
 $Q_{B3} = 1/180 = 0.0055$   
 $R_{B3} = 1 - Q_{B3}$   
 $= 1 - 0.0055 = 0.9945$
- 5) The probability of engine maintenance (QB4) and the reliability (RB4)  
 $Q_{B4} = 1/720 = 0.00139$   
 $R_{B4} = 1 - Q_{B4}$   
 $= 1 - 0.00139 = 0.9986$
- 6) The probability of generator operation failure (QB5) and the reliability (RB5)  
 $Q_{B5} = 1/180 = 0.0055$   
 $R_{B5} = 1 - Q_{B5}$   
 $= 1 - 0.0055 = 0.9945$
- 7) The probability of (ATS) operation continuously failure (1-R<sub>SS</sub>)

$$(1 - R_{SS}) = 1/720 = 0.00139 \rightarrow R_{SS} = 0.9985$$

And the Probability of (ATS) switching failure

$$Q_S = 1/360 = 0.00278 \rightarrow P_S = (1 - 0.00278) = 0.9972$$

Using formula (6), the Hybrid system reliability is

$$R = R_S(1 - (Q_A - Q_A P_S(1 - Q_B)))$$

$$R = 0.99985(1 - (0.167 - 0.167 * 0.9972(1 - 0.06)))$$

$$= 0.988$$

Table (2) shows calculated reliability & non-reliability ratios of components in the hybrid system

Table (2)  
 The reliability & non-reliability ratios of components in the hybrid system

$Q_A$	0.167
$Q_{B1}$	0.033
$Q_{B2}$	0.017
$Q_{B3}$	0.0055
$Q_{B4}$	0.00139
$Q_{B5}$	0.0055
$Q_B$	0.06
$1 - R_{SS}$	0.00139
$R_A$	0.833
$R_B$	0.94
$P_S$	0.9972
$R_{SS}$	0.9985

## 8. DISCUSSION

- 1) The readings shown in Table (1) show that the operation of the system continued uninterrupted to provide load with electric power, with a slight change in AC side voltage between the discharge state (227) volts and the charging state (229) volt. This does not affect the regularity of load work, and a break down of the power outage is not recorded during the conversion period.
- 2) The (ATS) operates when inverter input voltage become (46.1) volt and output voltage (227) volt, that is mean the battery is close to becoming discharged where the generator start generation then switching to load.
- 3) When the voltage of the batteries reaches the maximum value (51.5) volts, the load processing is switched from the generator to the photovoltaic system directly to ensure the continuity of electric feeding without interruption, and this proves the stability of the system with generator shut down.

From above, it is noticed the continuous providing of electric power with its parameters stability (Voltage, Current), Depending on the circuit components quality, which depends on the complexity of the manufacture and its origin and accuracy of specifications in proportion to the nature of loads. When looking at the load specifications (1 kW) and the specifications of the generator which is (5kW), that is to ensure providing the load with complete power with the battery recharging energy.

Table (2), is showing the reliability and non-reliability of the hybrid system, it is clear that the work of the hybrid system is more supported by the use of two systems rather than one single system. The main photovoltaic system reliability is (0.833) due to frequent cloudy days only, not due to unexpected failures or emergencies or large maintenance procedures, and the backup system reliability (generator system) is (0.94) depending on the quality of its components despite traditional maintenance procedures, but The reliability of the hybrid system (0.988) is greater than the reliability of the main system and the emergency system.

If the hybrid system is operating in days not cloudy or dusty, the non-reliability of the photovoltaic system is zero and its reliability is one. Thus, the hybrid system is operating with no need to an emergency system and the completion of the task with the reliability of its value is also one.



## 9. CONCLUSION

- 1) It is concluded that the occurrence of the faults mentioned above in the (faults that affect the components of the hybrid system) had an impact in determining the reliability of the system, and reducing its impact leads to raising the reliability of the system as follows:
- 2) Reducing the dust effect by cleaning photovoltaic surface, battery voltage monitoring, are reducing number of generator operation which results in fewer maintenance procedures, and thus increases the reliability of the generator, which increases the reliability of the hybrid system.
- 3) Using the component, spare parts, provided from Global and safe origin that is approve system high quality and reliability.
- 4) The increased reliability of the hybrid system means reducing maintenance costs, especially for the emergency system (electricity generator) in addition to reducing the necessary operating expenses of fuel and spare parts. This leads to the economic feasibility of the hybrid system.

## 10. REFERENCES

- [1] Demetri B. Kececioglu, "Reliability Engineering Hand Book" Volume2, 2002.
- [2] Roy Billinton & Ronald N. Allon, "Reliability Evaluation of Engineering Systems", Plenum press .Newyork and London 2003.
- [3] Wikipedia, "Failure Rates", websit, 2014.
- [4] R.C.Gupta and.M.Bradley, "Representing the mean Residual Life in Terms of Failure Rate", Department of Mathematics and Statistics, University of Maine, 2003.
- [5] Hermann Laukamp, "Reliability Study of Grid Connected PV Systems", IEA's PV Power Systems, 2002.
- [6] Timothy A. Loehlein "Maintenance is one key to diesel generator set reliability", Cummins Power Generation, 2007.
- [7] Gencontrol, "Automatic Transfer Switch Manual", 2013.



# Modeling and simulation for planar biped robot

Abbas Hussien Miry<sup>1</sup>, Ali Hussien Mary<sup>2</sup>, Gregor A. Aramice<sup>3</sup>

<sup>1,2,3</sup>Department of Electrical Engineering, University of Mustansiriyah

---

## ABSTRACT

---

The simulation of robotic system is becoming more general purpose to test the proposed system before implementation also it helps the designer to choose the better parameter in robot design. Also it provides information may be not available in hardware. Virtual reality is one of efficient simulation tools; especially it can be linked with Matlab which implement any algorithm using simulink and script files. In this paper mathematical model with the posture of the planar biped robot are simulated using matlab in the virtual environment to test its motion. Three points are taken (two feet and hip), these points decide the posture of biped robot by drawn of biped walking and save the (x,y) position for each point, then the equation of these motion are derived , Matlab 2014 is used as a programming tool with V-Realm Builder 2.0 It indicates that the simulation of MATLAB-based virtual reality design, reducing the design problems and make simple analysis.

---

## KEYWORDS

---

Virtual reality, matlab, biped, robot, modeling.

---

## ARTICLE INFO

---

Received 9 May 2019

Accepted 20 June 2019

DOI: 10.xxxxx

ISSN: 2413-0230

AL-MUHANDIS Journal (JMISE)

© 2018 Iraqi Society of Engineers (ISE)

E-mail: [jmise@ise-iq.org](mailto:jmise@ise-iq.org)

Online: [www.jmise.ise-iq.org](http://www.jmise.ise-iq.org)

Office Address: Iraq, Baghdad, Al-Nidhal Q.,103-30-5

---

## CORRESPONDING AUTHOR

---

Name: Abbas Hussien Miry

Email: [abbasmiry83@uomustansiriyah.edu.iq](mailto:abbasmiry83@uomustansiriyah.edu.iq)

Research Field:

Google Scholar:

---



### 1. INTRODUCTION

In Biped robot has a higher mobility of robots with another type of wheels robot, when moving over rugged ground, and obstacle avoidance [1]. Walking simulation, pattern helps to assess the movement of the robot without actual systems. Through simulation prior study with real robot, make the biped robot perform reliable movement, and it has helped the robot to find and prevent some of the potential problems during the actual experiences [2]. Biped robot design starts with simulation of the movement of the system. Then it developments of kinetic and dynamic simulation models, structural design, and the completion of the design of the robot controller. This simplified approach allows easy repetition of the design process at any step. This product allows the developer to choice optimal parameter for robot system to the maximum extent possible .At this stage, virtual reality technologies can simulate the process and interaction providing an immersive experience in real situations without real risk [3]. In recent year some work attends a virtual reality to simulate the system with Matlab, M.Z. Al-Faiz [4] used Matlab with Simulink and virtual reality for the posture of the robotic arm to perform the human arm motion, B. Lee et al [2] use Virtual Reality Toolbox to simulate humanoid robot. M.Z. Al-Faiz [5] present simulation of human arm with direct kinematics, inverse kinematic and the dynamics. This paper presents a model of biped robot based on its gate and simulate its motion in Matlab/Simulink and virtual reality.

### 2. VIRTUAL REALITY TOOLBOX

Simulink 3D animation is the solution to interact with virtual reality models of the changing time dynamical systems. And extends the capabilities of MATLAB and SIMULINK program in the virtual reality world of graphics. 3-D provides a better development, and the work environment for the implementation of visual simulations. Key features of this product can be are:

Virtual worlds - to create virtual worlds by using Virtual Reality Modeling Language (VRML) technology. Dynamic Systems - to create and identify dynamical systems with MATLAB Manipulation - to change attitudes and characteristics of objects in the virtual Interaction - interaction with the dynamic models of the virtual environment [6].

### 3. PROPOSED METHOD

The proposed method contains some stages:

1) Mathematical model of biped posture :There are eight states of biped motion when it's moving from point to point as shown in figures 1 and 2 at every state the location of the feet and bib are concluded: at state 0 the position of the first foot computed from a triangle with angle =  $\theta/2$ ,  $x_f =$  opposite side therefore it equal to  $L \cdot \sin(\theta/2)$ , if the = length of biped leg -adjacent side therefore it equal to  $L \cdot \cos(\theta/2) = L \cdot (1 - \cos(\theta/2))$ , similarity the other position can be computed.

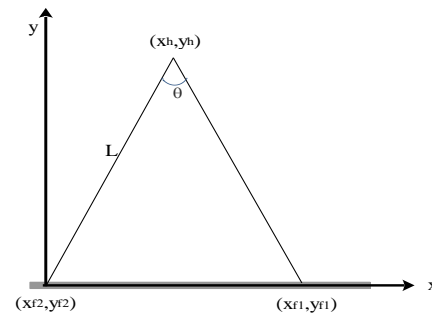


Fig.1 planar biped robot

Table .1 x-y coordinat of biped feet and hip

State		First foot Position		Hip position		Second foot Position	
i	j	xf1	yf1	xh	yh	xf2	yf2
0	0	$L \cdot \sin(\theta/2)$	$L \cdot (1 - \cos(\theta/2))$	0	L	0	0
	1	$2L \cdot \sin(\theta/2)$	0	$L \cdot \sin(\theta/2)$	$L \cdot \cos(\theta/2)$	0	0
	2	$2L \cdot \sin(\theta/2)$	0	$2L \cdot \sin(\theta/2)$	L	$L \cdot \sin(\theta/2)$	$L \cdot (1 - \cos(\theta/2))$
	3	$2L \cdot \sin(\theta/2)$	0	$2L \cdot \sin(\theta/2)$	L	$2L \cdot \sin(\theta/2)$	0
	4	$2L \cdot \sin(\theta/2)$	0	$2L \cdot \sin(\theta/2)$	L	$3L \cdot \sin(\theta/2)$	$L \cdot (1 - \cos(\theta/2))$
	5	$2L \cdot \sin(\theta/2)$	0	$3L \cdot \sin(\theta/2)$	$L \cdot \cos(\theta/2)$	$4L \cdot \sin(\theta/2)$	0
	6	$3L \cdot \sin(\theta/2)$	$L \cdot (1 - \cos(\theta/2))$	$4L \cdot \sin(\theta/2)$	L	$4L \cdot \sin(\theta/2)$	0
1	7	$4L \cdot \sin(\theta/2)$	0	$4L \cdot \sin(\theta/2)$	L	$4L \cdot \sin(\theta/2)$	0
	0	$5L \cdot \sin(\theta/2)$	$L \cdot (1 - \cos(\theta/2))$	$4L \cdot \sin(\theta/2)$	L	$4L \cdot \sin(\theta/2)$	0
	1	$6L \cdot \sin(\theta/2)$	0	$5L \cdot \sin(\theta/2)$	$L \cdot \cos(\theta/2)$	$4L \cdot \sin(\theta/2)$	0
	2	$6L \cdot \sin(\theta/2)$	0	$6L \cdot \sin(\theta/2)$	L	$5L \cdot \sin(\theta/2)$	$L \cdot (1 - \cos(\theta/2))$
	3	$6L \cdot \sin(\theta/2)$	0	$6L \cdot \sin(\theta/2)$	L	$6L \cdot \sin(\theta/2)$	0
	4	$6L \cdot \sin(\theta/2)$	0	$6L \cdot \sin(\theta/2)$	L	$7L \cdot \sin(\theta/2)$	$L \cdot (1 - \cos(\theta/2))$
	5	$6L \cdot \sin(\theta/2)$	0	$7L \cdot \sin(\theta/2)$	$L \cdot \cos(\theta/2)$	$8L \cdot \sin(\theta/2)$	0
6	$7L \cdot \sin(\theta/2)$	$L \cdot (1 - \cos(\theta/2))$	$8L \cdot \sin(\theta/2)$	L	$8L \cdot \sin(\theta/2)$	0	
7	$8L \cdot \sin(\theta/2)$	0	$8L \cdot \sin(\theta/2)$	L	$8L \cdot \sin(\theta/2)$	0	

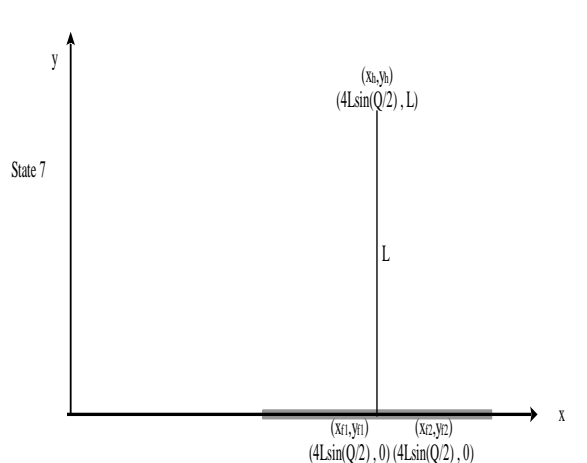
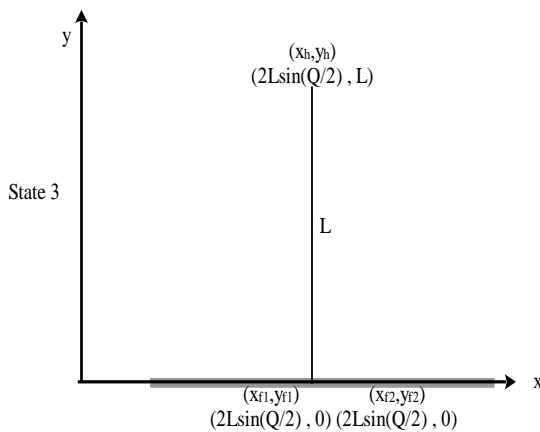
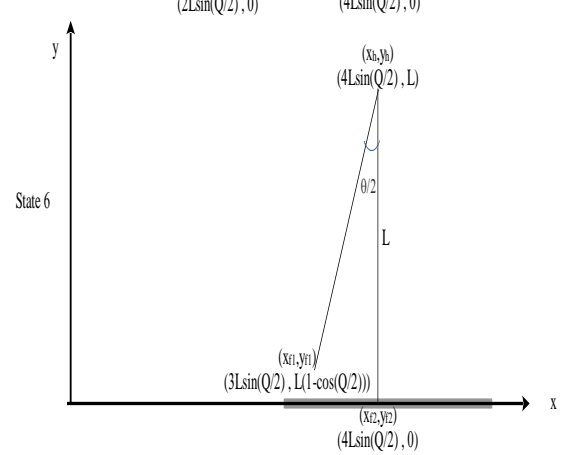
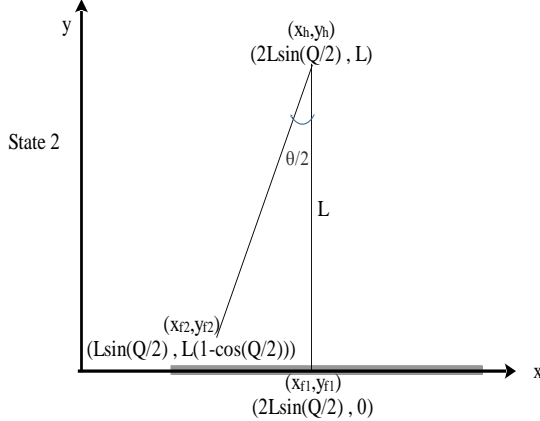
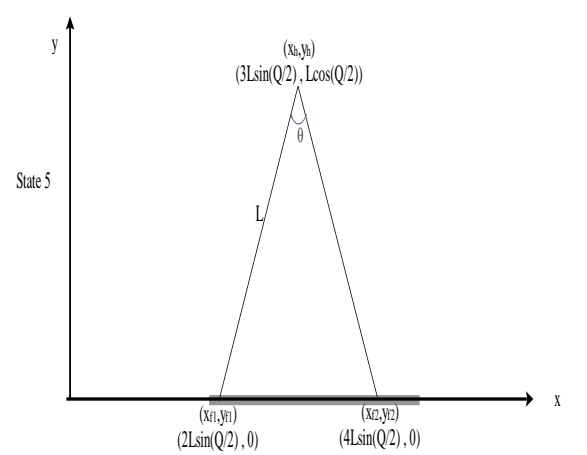
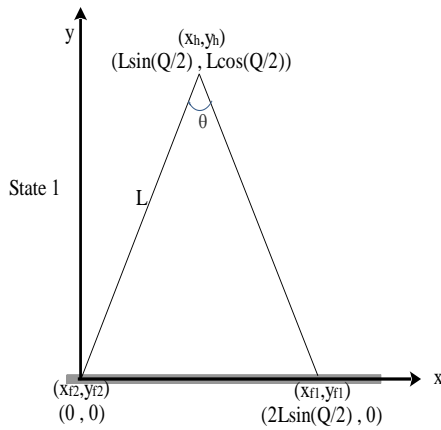
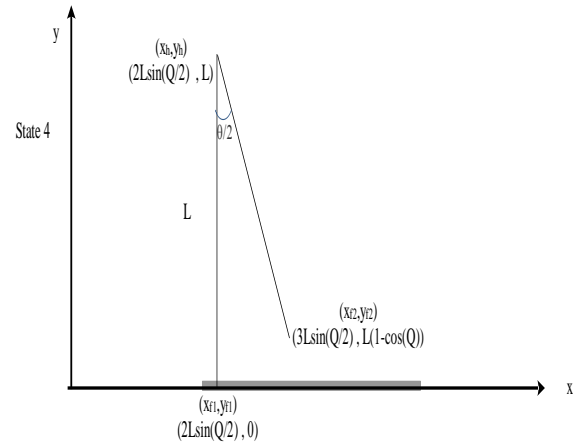
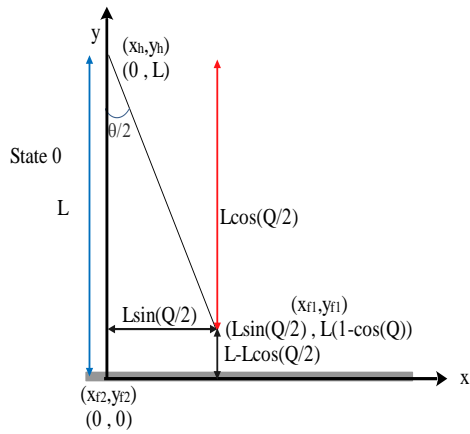


Fig.2 Gait cycle of planar biped robot

Fig.2 (continued) Gait cycle of planar biped robot



From the table it can be conclude the equation of biped motion with following equations

$i = 0:N$   $N$  refer to number of running state

which reach to infinity

$j = 0:7$  Biped robot repeat it motion every 8 states

$$X_{f1} = \begin{cases} (4i + 1)L\sin\left(\frac{\theta}{2}\right) & j = 0 \\ (4i + 2)L\sin\left(\frac{\theta}{2}\right) & j = 1:5 \\ (4i + 3)L\sin\left(\frac{\theta}{2}\right) & j = 6 \\ (4i + 4)L\sin\left(\frac{\theta}{2}\right) & j = 7 \end{cases} \quad (1)$$

$$Y_{f1} = \begin{cases} L\left(1 - \cos\left(\frac{\theta}{2}\right)\right) & j = 0,6 \\ 0 & \text{else} \end{cases} \quad (2)$$

$$X_h = \begin{cases} 4iL\sin\left(\frac{\theta}{2}\right) & j = 0 \\ (4i + 1)L\sin\left(\frac{\theta}{2}\right) & j = 1 \\ (4i + 2)L\sin\left(\frac{\theta}{2}\right) & j = 2:4 \\ (4i + 3)L\sin\left(\frac{\theta}{2}\right) & j = 5 \\ (4i + 4)L\sin\left(\frac{\theta}{2}\right) & j = 6:7 \end{cases} \quad (3)$$

$$Y_h = \begin{cases} L\left(1 - \cos\left(\frac{\theta}{2}\right)\right) & j = 1,5 \\ 0 & \text{else} \end{cases} \quad (4)$$

$$X_{f2} = \begin{cases} (4i)L\sin\left(\frac{\theta}{2}\right) & j = 0 \\ (4i + 1)L\sin\left(\frac{\theta}{2}\right) & j = 1 \\ (4i + 2)L\sin\left(\frac{\theta}{2}\right) & j = 2:4 \\ (4i + 3)L\sin\left(\frac{\theta}{2}\right) & j = 5 \\ (4i + 4)L\sin\left(\frac{\theta}{2}\right) & j = 6:7 \end{cases} \quad (5)$$

$$Y_{f2} = \begin{cases} L\left(1 - \cos\left(\frac{\theta}{2}\right)\right) & j = 0,6 \\ 0 & \text{else} \end{cases} \quad (6)$$

Where  $\theta$  is angle between biped foot , $L$  is length of leg , $i,j,N$  are counter of state ,

2) Matlab

The equations is written in script file in Matlab and apply a different value of  $\theta$  ,fig's (3-4) show the planner biped motion for angle=20 and 40 , the red line represent the hip motion of biped robot, from the figures it can be shown the large angle produce long distance but with variations in the hip which make the motion is unstable

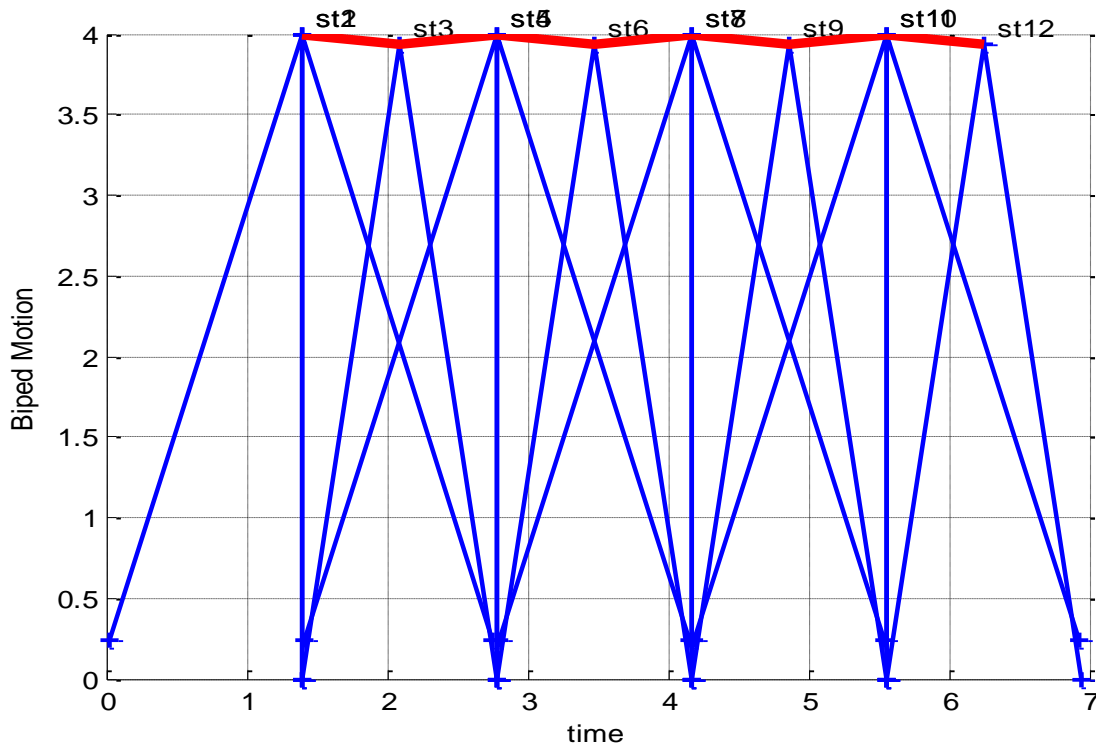


Fig.3 biped robot posture using script file with  $\theta = 20$

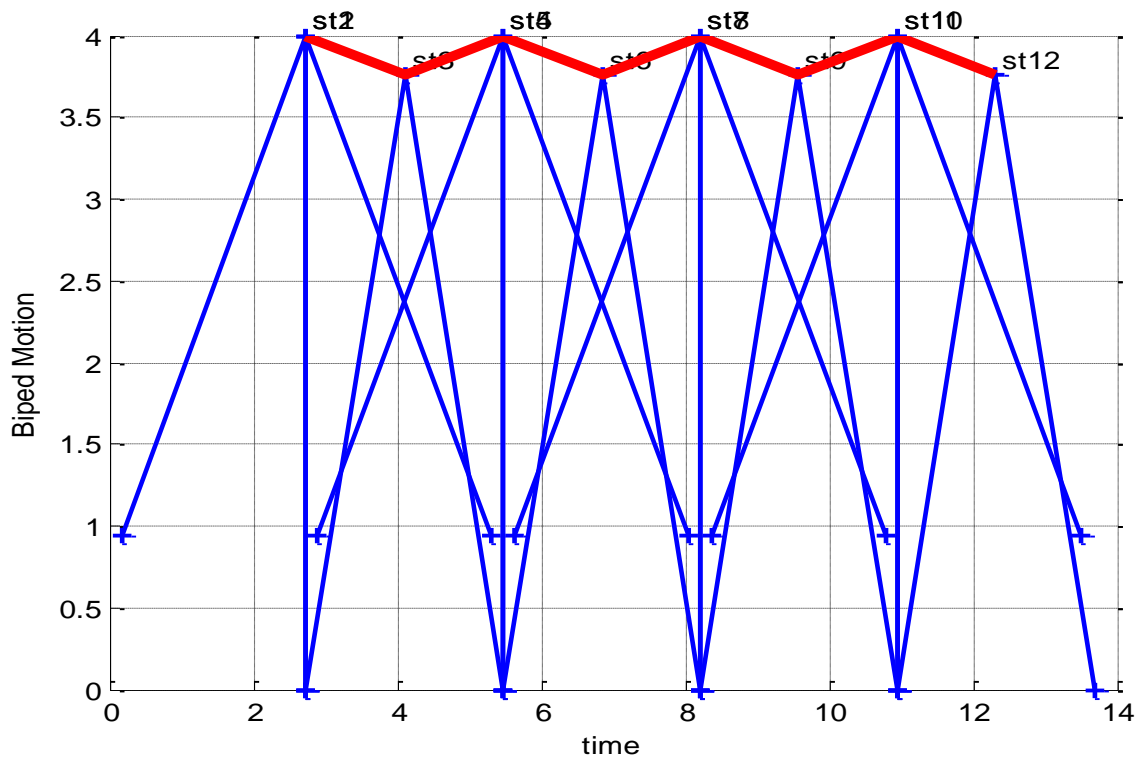


Fig.4 biped robot posture using script file with  $\theta = 40$

#### 4. VIRTUAL REALITY

Application development in robotics requires defining the task to be performed accurately to determine the required characteristics of the robot. To determine these parameters, task execution can be divided into the following steps: 1) Modeling phase, at this stage, it is necessary to model the three-dimensional robot in a computer-aided design (CAD) program. The model allows the analysis of the physical properties of the robot before the construction, (2) the construction phase, the main objective of this stage is to assemble all the mechanical parts designed and integrate the necessary electronics to move each joint, (3) phase controllers design, to design advanced control algorithms, Mathematical dynamics representing dynamics and dynamics. Software tools that work to solve mathematical matrix operations to facilitate the implementation of the proposed control scheme are required. Matlab is a tool with its own programming language and a development environment that provides matrix processing and data manipulation. (4) Simulation Phase before the

time

experimental algorithms of the proposed control algorithms are implemented, it is necessary to

verify their performance in a 3D environment that simulates the actual conditions in which the robot operates, , Virtual development tools are required with the ability to support dual offset devices, among other things. Successful implementation of the planned task depends on compliance with each of the above detailed step objectives. In this context, one can say that the design and simulation of control algorithms are the most important stages of task performance, so this work focuses on these two elements.

Virtual reality is used in this paper to simulate and show the motion of the planar biped robot in 3-D which makes the analysis of problem near

a) VRML: in this step the biped robot is built using VRML software as shown in the figure, below

b) Animate the body which built in the previous step by link VRLM file with Matlab in Simulink that contain virtual reality tools such sink and other simulink model of biped to real system.:

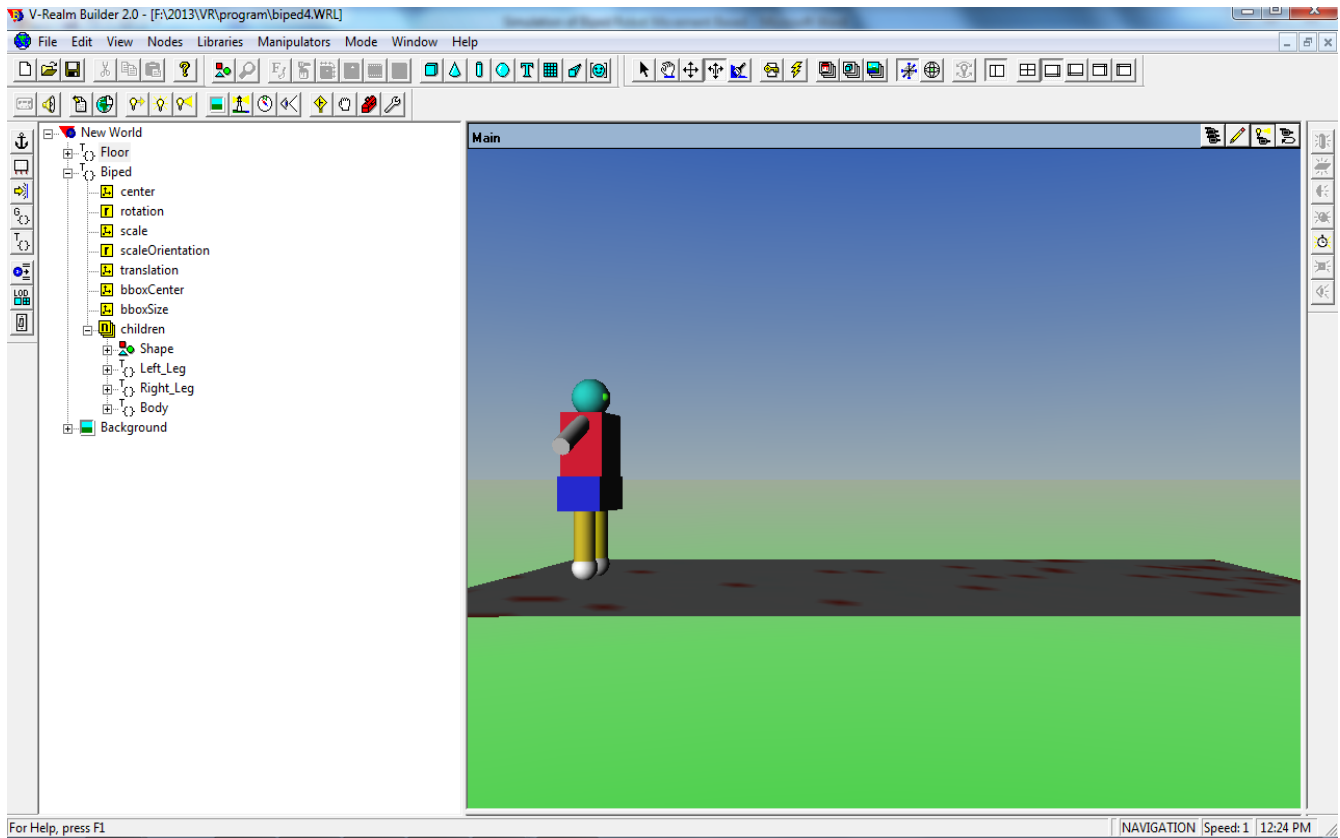


Fig.5 Biped robot in VRML format

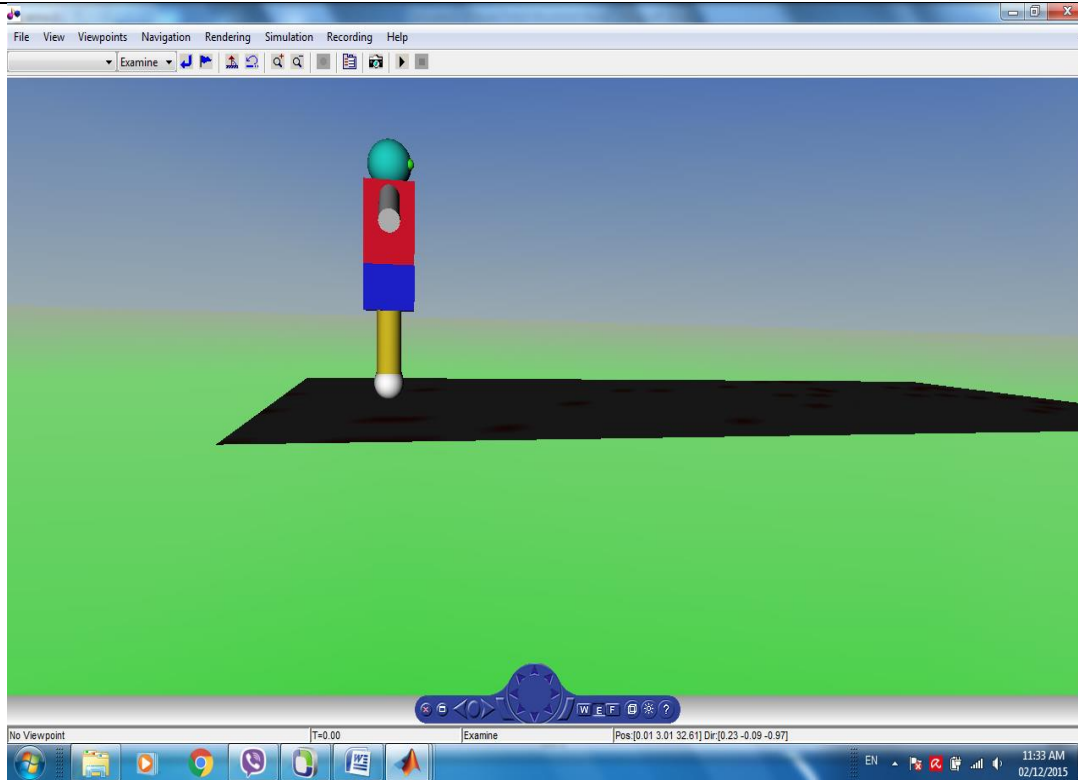


Fig.7 Virtual Reality output of the biped robot simulation

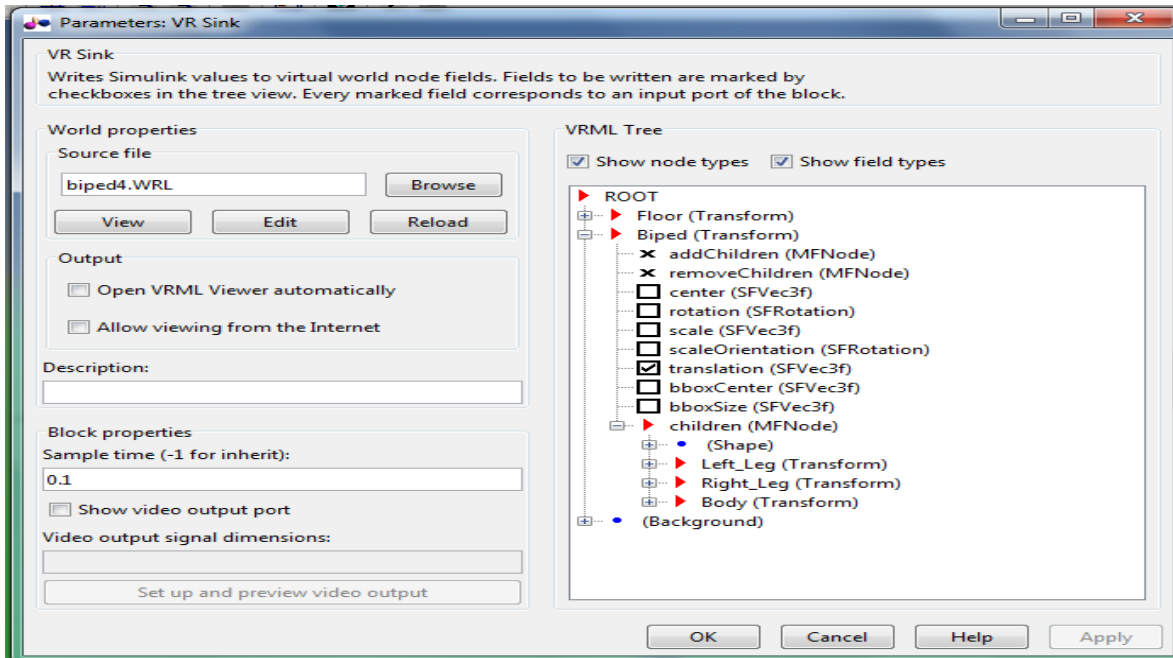


Fig.8 VR sink block parameter window

C) After apply equation (1 to 6) in a script file and apply in simulink to animate the biped body using virtual reality.

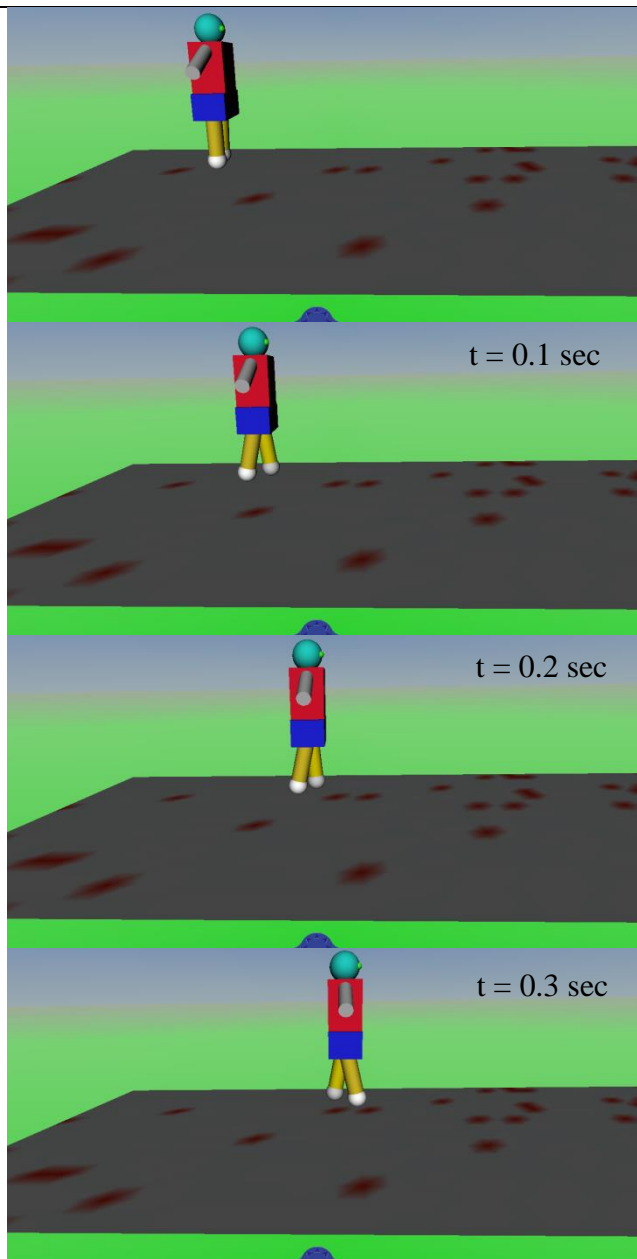


Fig.9 A snapshot of the biped motion in the virtual reality.

From above figures it be noted that, the motion in virtual reality is equivalent to the motion in fig.3 and fig.4. However there a small difference between actual robot with simulated robot due to physical component in actual robot.

## 5. CONCLUSION

This paper presented an easy way to create a model for planar biped robot using VRML and matlab, which forms a support tools during development and design complex mathematical models, with time and effort savings in the process, the planner biped robot movements made in the virtual matlab environment, have proved satisfactory results by test robot posture using different value of angle between biped foot taking advantage of MATLAB functions of modeling.

It can be concluded that this simulation helps the designer to test the different angle of motion and posture for biped robot, also this paper shows the benefit of virtual environment tool that help researcher to visualize the system dynamic with motion of biped robot and the join it with environment . The simulation of MATLAB-based virtual reality, reducing the design problems and offer simple analysis. In future work it is possible to optimize the angle of motion using artificial intelligent algorithm.

## 6. REFERENCE

- [1] M. Fevre ,B. Goodwine and J. P. Schmiedeler , "Design and Experimental Validation of a Velocity Decomposition-Based Controller for Underactuated Planar Biped", IEEE Robotics and Automation Letters ,Vol.3, Issue. 3, 2018
- [2] Lee .B, Kim .Y, Yoo .J, Park .I and Kim .J, 2008, "Walking Pattern Simulation based on Virtual Reality Toolbox", 2007 FIRA Robot World Cong conf., USA, 2007.
- [3] L. Perez, E. Dieza, R. Usamentiaga and D.García, " Industrial robot control and operator training using virtual reality interfaces ", Computers in Industry ,Vol.109 PP:114–120, 2019.
- [4] Al-Faiz ,M.Z," A Posture Human Robotic Arm by Inverse Kinematic With Virtual Environment", MASAUM Journal of Basic and Applied Sciences, Vol.1, No. 4,
- [5] Al-Faiz ,M.Z, Abduladhem A. Ali, Abbas H.Miry, " Human Arm Simulation Based on MATLAB Simulink with Virtual Environment", IJCCCE, Vol.11, NO.1 ,pp:86-96 , 2011
- [6] D. Todorović<sup>1</sup>, M. Božić<sup>1</sup>, V. Zerbe, G. S. Đorđević<sup>1</sup> , " Virtual Reality Interface in MATLAB/SIMULINK for 2DOF Joystick Control " Automatic Control and Robotics Vol. 9, No 1, 2010, pp. 87 – 94.



---

# Effective adaptive filtering method for salt-and-pepper noise reduction in computed tomography images

Abbas Hussien Miry

Department of Electrical Engineering, University of Mustansiriyah

---

## ABSTRACT

Removing noise from medical images is very difficult to process images. In recent years, technological development has improved dramatically in the medical imaging analysis. There are several effective de-noising methods such as median filtering that used for removing the impulse noise. However, the median filters, return each pixel with a median value, regardless of whether it was a noise or clean of blurring pixels exhibits filter images. This paper introduces a new filtration technique to eliminate the salt and pepper noise of from medical Computed Tomography (CT) .It proposed to improve the median filtering by changing the shape of windows to make the result pixel is closed to the original value as much as a possible match. The Experimental results of the noisy CT lung image show that the performance of the proposed method outperforms the other methods in terms of visual quality, PSNR and MAE, Even when the noise level reaches 40%.

---

## KEYWORDS

CT image, salt and pepper, noise, median filter, adaptive median filter.

---

## ARTICLE INFO

Received 9 May 2019

Accepted 20 June 2019

DOI: 10.xxxxx

ISSN: 2413-0230

AL-MUHANDIS Journal (JMISE)

© 2018 Iraqi Society of Engineers (ISE)

E-mail: [jmise@ise-iq.org](mailto:jmise@ise-iq.org)

Online: [www.jmise.ise-iq.org](http://www.jmise.ise-iq.org)

Office Address: Iraq, Baghdad, Al-Nidhal Q.,103-30-5

---

## CORRESPONDING AUTHOR

Name: Abbas Hussien Miry

Email: [abbasmiry83@uomustansiriyah.edu.iq](mailto:abbasmiry83@uomustansiriyah.edu.iq)

Research Field:

Google Scholar:

---



## 1. INTRODUCTION

In the daily routine, digital imaging is a vital task, and is used in CCTV and access control, and medicine systems. Representation of medical images in digital play an necessary role in medical diagnostics, such, computer tomography (CT), magnetic resonance image , etc. with the recent growth in health, medicine, increasing interest medical research and image processing. The importance of high accuracy in medical image cannot be exaggerated. Thus, the digital restoration of images is an important element in the treatment of medical images. The restoration of image refers to the existence of a picture which environmental degradations include removing the original noise restore/clean image [1].

During the examination of the samples and transfer, quantifying the image, usually contaminated types of noise outside which makes the picture does not reflect the reality of the scenery to the detriment of the quality of the Image. There are types of noise are familiar: Gaussian noise, such as transmission noise channel. The other is the Speckle noise like salt and pepper noise, which mean the white noise in the form of a black or a black point in the image. In the case of digital data traffic, compared to Guass noise salt & pepper is the main reason leading to the error. Therefore, in order to impact noise especially denoising minis batch pre-process noise on contaminated image [2]. Median filtering is simplest ways to remove impulse noise using window filter ,however, the traditional median filters, reaffirming each pixel with median value regardless of whether it was a noise or clean of blurring pixels exhibits filter images[3].

Recently, Toh[3] proposed the noise adaptive fuzzy switching median (NAFSM) filter. NAFSM filter a hybrid between the fuzzy switching median filter and adaptive median filtering, to expand the size of the window filter according to the noise density. Sun[2] combines the adaptive median filter with improving weight mean filter to preserving the edge of the image, Chang [4] use the threshold level and median filter to detect the noise and change the value of the original pixels closer to the latest or the same level of the median value. Turajli[5] use the neural network to Computed Tomography (CT) image denoising. Z. Li [6], Develop and evaluate the noise reduction method in the image field based on modification Non-localized (NLM) algorithm that adapts to local CT noise level and to its implementation, This method in a time frame is consistent with the clinical workflow. G Elaiyaraja[7] proposed Trimmed Median (TM) filter to remove fixed high-density pulse noise in CT image. It

is proposed to scan images and sequence of colored video in the abdomen.

In this paper the filtering process is apply on special area of window not on all pixel value ,to make the new value is nearest to the original gray level.

## 2. IMPULSE NOISE

Impulse noise occurred during take photos because of the conversion or temperature sensor may occur as a result of the intervention of the channel or due to weather disturbances during the video transmissions. It is uncorrelated independent image pixels are always distributed randomly on the picture. Each pixel does not damage, some pixels in the image of the CT scan may damage with impulse noise.

Impulse noise can be of different types, salt and pepper and random value noise. Salt and pepper type of impulse noise either the value or the salt and pepper. The value of pixel in salt can be either 0 or 255. Black and white spots appear on the image containing the salt and pepper type of impulse noise [8].

## 3. ADAPTIVE MEDIAN FILTER

In median filter, there is a square window, the window size variable. The centre pixels in scan window must be denoised, the first step is to sort each pixel in current window; the second step is to change the value to the median level of the sorting sequence. The median filter is a simple and effective technique to remove the noise had continued in use for a time [4].

Unlike the median filter the window size in adaptive median filter is changing according to the size of image. In the adaptive median filter, the noise density controls the size of window. The problem of blurring in edge which appears in median filter can be overcome by using adaptive median filtering the size of the window is varying according to noise density [9].

Window size in the adaptive median filtering is not fixed in size vary as a result of the pixels representing the average pixels within the current window. If the median value of the pixels is noisy, then expand the size of the window. Otherwise, a further treatment on the part of the image, surrounded by the current window [10].

## 4. MODIFIED ADAPTIVE MEDIAN FILTER

Inspect the advantage of AMF with variation of window size but increasing window size in AMF all the pixel in the window are taken ,which effect on the



median value ,in this paper only the surrounding pixel are taken in sorting as circle form ,the producer of proposed method:

$S_{xy}$  =window size

$S_{max}$  =maximum **window** size

$Wmin$ =minimum level in current window

$Wmax$ =maximum level in current window

$Wmed$ =median level in current window

$I_{xy}$ = input image value at coordinate (x,y)

$P_{xy}$ = processed image value at coordinate (x,y)

Step 1: Calculate  $Zmin$ ,  $Zmax$  and  $Zmed$  for the window define by the following equations

$$S = \begin{cases} 1 & (i + j) > V1 \ \& \ (i + j) < V2 \\ & \ \& \ (i - j) < V1 \ \& \ (i - j) < V1 \\ 0 & \text{otherwise} \end{cases} \quad (1)$$

$$V1 = (S_{xy} + 1)/2 \quad (2)$$

$$V2 = 3. (S_{xy} + 1)/2 \quad (3)$$

The result window shown in fig.1-3, the shaded area mean the filtering apply on the special area in window (shading) ,this step is applied to make the new value effected by the surrounding pixel only which make the new value nearest to the original value.

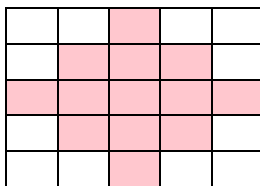


Fig.1 5x5 window

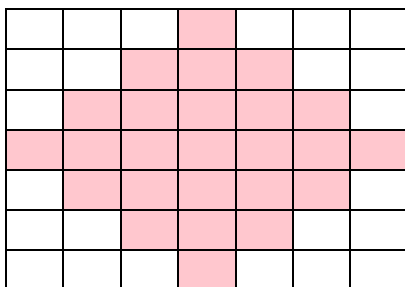


Fig.2 7x7 window

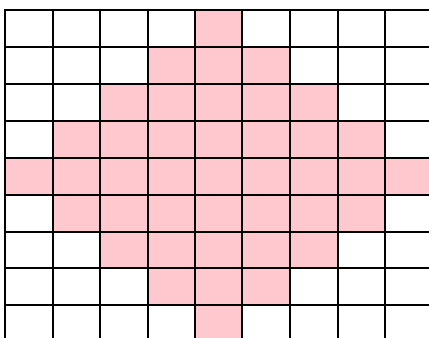


Fig.3 9x9 window

Step 2: Test the condition

$(Wmin < Wmed < Wmax)$

- True: go to step 3

- False:

Increase the window size and return to step 2.

Step 3:

Test the condition

$(Wmin < I_{xy} < Wmax)$

$R_{xy} = Wmed$

(4)

## 5. SIMULATION RESULT

In our experiments, the original 512x512, 8 bits/pixel CT images from a database of the DICOM of NSCLC Database. The result of all method can be performed by using different noise level, increasing the noise density from 10% to 40% and processing this image by using different method:

MAMF: Modified Adaptive Median Filter

AMF: Adaptive Median Filter

NAFSM: Noise Adaptive Fuzzy Switching Median Filter.

MD: Median Filter

For the result evaluation, we can use different measures of quantity and an assessment of the quality of the renovation process. It is the mean absolute error (MAE) peak signal-to-noise ratio (PSNR).These definitions are provided below [5].

$$MAE = \frac{\sum_{i=0}^{K1-1} \sum_{j=0}^{K2-1} |I(i,j) - \hat{I}(i,j)|}{K1.K2} \quad (5)$$

$$PSNR = 10. \log \frac{M.N.V^2}{\sum_{i=0}^{K1-1} \sum_{j=0}^{K2-1} [I(i,j) - \hat{I}(i,j)]^2} \quad (6)$$

Where

$V$  The level of the density of the image which equal to 255 .

$\hat{I}(i, j)$  the reconstructed image

$I(i, j)$  the original image

The assessment of the results displayed in Fig. 4-6 and tables 1-2.

Table.1 Average PSNR for different methods and noise density for 25 CT image

Method	Noise Density			
	10%	20%	30%	40%
MAMF	40.2945	37.6501	35.7269	33.4584
AMF	36.7931	35.9369	33.5100	31.7764
NAFSM[3]	34.8937	32.7570	29.0268	27.5247
MD	30.7806	29.0875	27.8380	26.8379



Table.2 Average MAE for different methods and noise density for 25 CT image

Method	Noise Density			
	10%	15%	20%	30%
MAMF	0.7805	0.8059	0.8530	0.9947
AMF	0.9558	1.0377	1.2901	1.6441
NAFSM[3]	0.7487	1.1227	1.8351	2.3669
MD	2.0217	2.4092	3.1345	4.7628

details and choice good position of pixel in the filter

PSNR and MAE curves (Fig.4-5) in the presence of noise demonstrate that, the proposed method is better from other existing methods. Fig. 6 shows the results for the various methods of denoising on the test image with 40% noise density of salt and pepper. Median filter keeps the details of the image, but a some of noisy pixel are appear in the image. NAFSM and adaptive media filter are having good filtering but there is a distortion in some region of proceeds image, the proposed method has better quality. It can be remove the noise while maintaining the details of the image.

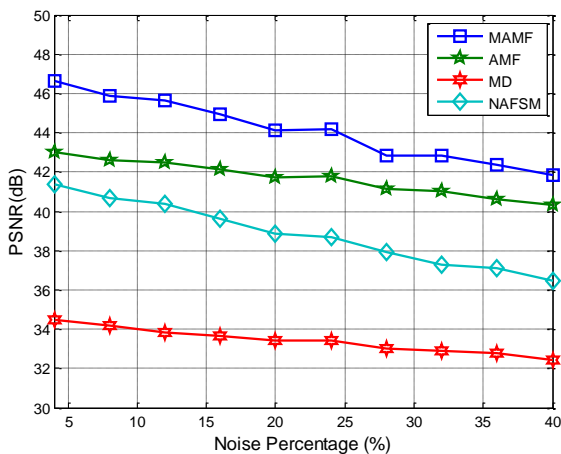


Fig.4 Comparison of different methods with respect to noise density in term PSNR

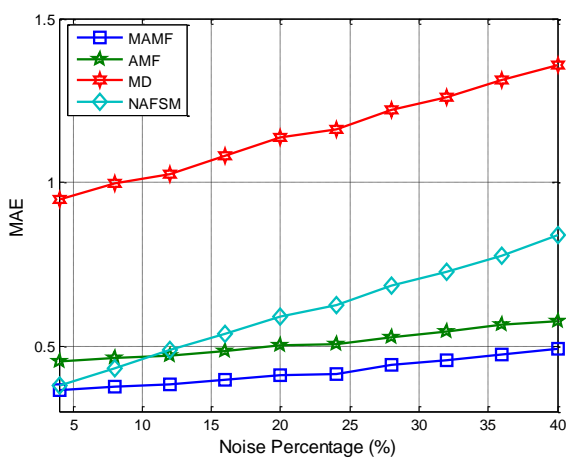
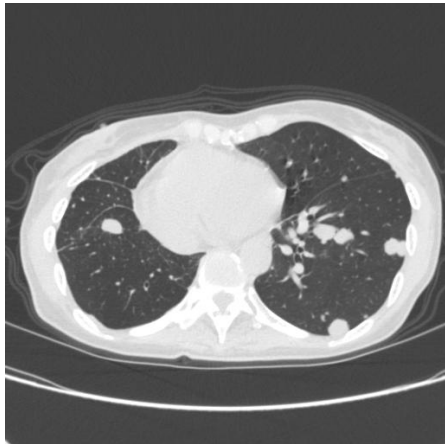
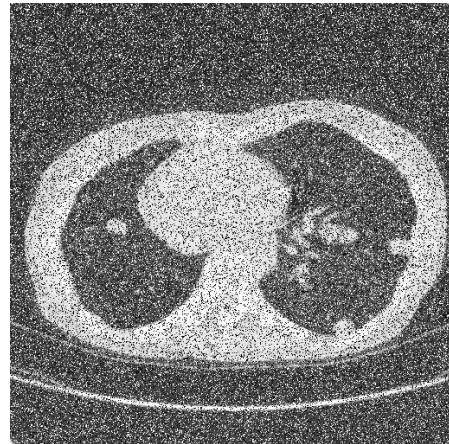


Fig.5 Comparison of different methods with respect to noise density in term MAE



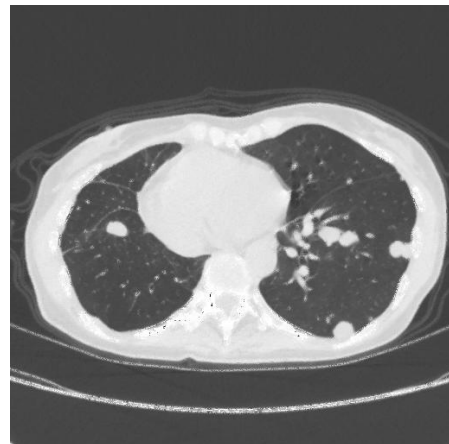
(a) Original image



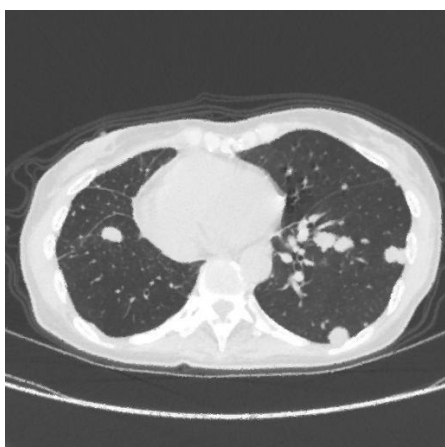
(b) Noised image



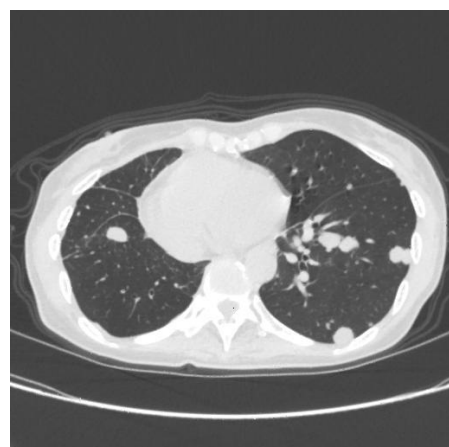
(c) Denoised image based Median filter



(d) Denoised image based fuzzy



(e) Denoised image based adaptive median filter



(f) Denoised image based modified adaptive median filter

Figure 6.Result images



## 6. CONCLUSION

A simple method is presented in this paper to improve the adaptive median filter to get best denoising performance. The adaptive filtering process was applied to special areas of the window not on all pixel value. In this paper the shape of window is vary to make the new value of new pixel is nearest to the original gray level as much as possible. It can be concluded that, This method more suited for the denoising of the CT image corrupted by salt and pepper noise, it found that the proposed method revealed better performance in term PSNR and MAE and preserve the CT edge. This result makes it an effective filter tool for use against salt and pepper noise. In future work, the research should, focus on the shape of window with more

## 7. REFERENCES

- [1] Elhoseny M. and Shankar K., "Optimal Bilateral Filter and Convolutional Neural Network based Denoising Method of Medical Image Measurements", elsevier Measurement Vol. 143, PP:125-135 ,2019.
- [2] S. Garg, R. Vijay and Shabana Urooj , "Statistical Approach to Compare Image Denoising Techniques in Medical MR Images", elsevier Procedia Computer Science, Vol.152, pp:367-374 ,2019.
- [3] Kal K. Toh .V and Ashidi N., "Noise Adaptive Fuzzy Switching Median Filter for Salt and Pepper Noise Reduction" , IEEE Signal processing letters , Vol. 17, No. 3, pp:281-284 ,2010.
- [4] Chang C., Hsiao J. and Hsieh C., "An Adaptive Median Filter for Image Denoising " , Second International Symposium on Intelligent Information Technology Application, Publisher: IEEE, pp: 346- 350 ,2008.
- [5] Mu W. , Jin J. and Feng H. , Wang Q. , "Adaptive Window Multistage Median Filter for Image Salt-and-pepper Denoising" , Instrumentation and Measurement Technology Conference , Publisher: IEEE, Print ISSN: 1091-5281, 2016.
- [6] Madhura J . and Babu R. , "A Survey on Noise Reduction Techniques for Lung Cancer Detection " , International Conference on Innovative Mechanisms for Industry Applications (ICIMIA), Publisher: IEEE ,pp: 637- 640 ,2017.
- [7] Z. Li ,L. Yu,J. Trzasko , " Adaptive nonlocal means filtering based on local noise level for CT denoising" , Med. Phys. Vol.41,No.1,PP: 1-16 , 2014
- [8] G Elaiyaraja, N Kumarathan, " An enhanced algorithm for removal of noise in CT scan image and 3D abdomen color video sequence through trimmed based filter" , Biomedical Research Vol. 28 ,No.2,PP: 512-518 ,2017.
- [9] Vispute .A. M., Rindhe B. U. and Shekoker .D. N. , "Efficient Adaptive Mean Filtration Technique in Denoising of Medical Imaging" , International Conference on Global Trends in Signal Processing, Information Computing and Communication, Publisher: IEEE, pp: 312- 315, 2016.
- [10] Altun A. A. and Mulki H., " Multistage Filtering Algorithm for Salt and Pepper Noise Removal from Highly Corrupted Microscopic Blood Images" ,International Research Journal of Electronics & Computer Engineering Vol .2,No.4,pp:11-16, 2016.



# On ultrasound elasticity imaging: investigation of correlation window length for breast phantom inclusion differentiation using ultrasound radiofrequency data

Ali.R.H. Al-jader<sup>1</sup>, Aws Al-azawi<sup>2</sup>, Taha Ahmed<sup>3</sup>

<sup>1</sup>Department of Medical Instrumentation Engineering Techniques, Middle Technical University

<sup>2</sup> Department of Medical Instrumentation Engineering Techniques, Middle Technical University

<sup>3</sup> Medical Imaging Sales Manager, Al-Mubda'a Scientific Company

## ABSTRACT

An ultrasound elasticity imaging introduced to illustrate mechanical characteristic of elasticity for tissue region of interest. Elastic map determined by similarity measurement of acquired radiofrequency data before and after applied compression. Similarity measurement algorithm of cross-correlation is widely used in image processing. In this study, an adjustment of correlation window length in addition to correlation window overlap is investigated to reduce outlier occurrence. The investigation is performed using ultrasound raw data that has been acquired during applied gentle freehand compression. Freehand compression is applied by ultrasound probe surface over breast phantom that includes hard inclusion. Range of correlation window length are considered in determination of the adjust processing parameters, where correlation window length of before applied compression are adjusted from 40-samples to 140-samples, while after applied compression are also investigated to be longer for the factor range from 1 (same length as window before compression) to 1.4. The investigation also includes range of overlap between sequential windows of 25%, 50%, and 75%. Results show that, displacement map with lower outlier occurrences from 40 to 80 window length with longer factor of 1.1 and window overlap 75%.

## KEYWORDS

Elasticity imaging, signal processing, ultrasound radiofrequency, breast phantom tissue, sonography.

## NOMENCLATURES

$V_1$  before compression window length, samples.  
 $F$  after compression window length, factor.  
 $W$  correlation window over lapping, ratio.  
 $C$  outlier occurrences, counter.  
 CCF cross correlation function, algorithm.

## ARTICLE INFO

Received 9 May 2019

Accepted 20 June 2019

DOI: 10.xxxxx

ISSN: 2413-0230

AL-MUHANDIS Journal (JMISE)

© 2019 Iraqi Society of Engineers (ISE)

E-mail: [jmise@ise-iq.org](mailto:jmise@ise-iq.org)

Online: [www.jmise.ise-iq.org](http://www.jmise.ise-iq.org)

Office Address: Iraq, Baghdad, Al-Nidhal Q.,103-30-5

## CORRESPONDING AUTHOR

Name: Dr. Aws Alazawi

Email:aws\_basil@mtu.edu.iq

Research Field: Biomedical Signal Processing

Google Scholar: <https://scholar.google.com/citations?hl=en&user=QzVrWTYAAAAJ>



## 1. INTRODUCTION

A world health organization has been recently reported that female breast cancer ranked as the fifth leading cause of death [1]. Medical imaging modalities of ultrasound, X-ray and MRI are routinely used for breast cancer diagnosis. In particular, the ultrasound considered as non-ionize and non-invasive with a capability to differentiate soft tissues [2], in addition to portability and low cost compared to X-ray and MRI. In ultrasound, tissue region of interest illustrated in form of sonogram that describes tissue heterogeneity, while recently tissue elasticity measured in term of sonoelastic map [3]. Elasticity imaging able to differentiate soft tissues based on mechanical properties, in which coherent scatterers exploited to measure these properties when regions stimulated by external or internal stress [4]. Strain map estimated by measure gradient displacement, in which acquired raw data of before and after stimulation are compared to determine similarity [5]. Initial study described the elastic map in one dimension as axial strain, which is subtle to the similarity loss due to decorrelation produces noisy strain image [6]. Axial stretching of post-compression frame was introduced to reduce the decorrelation noise. On the other hand, a lateral stretching was also considered in addition to axial one in terms of 2-D companding [7]. For 3D strain imaging 3-D companding investigated to increase similarity that is affected by scatter motion of incompressible material [8]. Further studies considered decorrelation noise reduction such as, adaptive stretching [9], 3D multi Compression [10], motion decorrelation [11], affine transformation [12], supervised classification [13]. On the other hand, window length has a significant contribution on decorrelation noise occurrence at an expense on axial resolution by the refinement process[14]. The aim of this study, is to develop a new signal-processing method that uses RF data for an estimation of elastic map of biological tissue, with the objective of moving from global to regional assessment of early detection of breast tissue. This study presents sonoelastic map for breast tumor, where axial displacement measured using cross correlation algorithm for range of window length to optimally adjust correlation parameters that provides certain axial resolution. The correlation parameters represented by before and after windows length are investigated using ultrasound radio-frequency data for breast phantom.

## 2. METHODOLOGY

Radiofrequency data are acquired using VINNO G55 ultrasound machine, where freehand compression was applied by probe physical surface on breast elastography Phantom CIRS model 059 [15]. The experiment was performed at research laboratory of Al-Mubda'a bureau in Baghdad-Iraq in a conjunction with research and development department of VINNO company. In [16], the research team acquired Radiofrequency ultrasound data using ultrasound research interface system, while in the VINNO G55 ultrasound clinic system was already designed to process Radiofrequency ultrasound data. In this study, the Radiofrequency data are acquired under a permission from VINNO research and development department according to the block diagram shown in figure(1), where the acquired channel lines are processed by beam-former for time compensation. Radiofrequency data represented by VINNO files are then converted to Matlab data using VINNO Matlab tool that considers VINNO machine parameters of 12MHz probe operating frequency and F4-12L broadband linear array transducer of 512 elements [17]. As a consequence, acquired radiofrequency data of before and after applied compression are processed according to the proposed algorithm represent by a flowchart shown in figure(2), to estimate displacement map of tissue region of interest at optimally adjusted correlation window length. In this algorithm a cross correlation technique represented by speckle tracking for displacement estimation is considered to investigate the optimal adjustment of correlation window length. The cross correlation function (CCF) used to measure the similarity between segment before and after applied compression. In which, peak correlation coefficient and accordingly its position determined using sub-sample differentiation of spline interpolation.

The positions of peak correlation confidants are then spatially converted to be as a displacement. As explained earlier, non-gradient displacement estimates are regarded as estimation outliers that would be reduced as much as possible by optimally adjusting correlation window length. As a result, correlation three parameters of before compression window length, after compression window length and sequential window overlapping are adjusted as in figure(3). In which, before window length is consider for the range from 40 to 140 samples, while after compression window length are longer than before one by the rate from 1 to 1.4, and also the sequential window overlapping is considered for ratio of from 0.25, 0.5, 0.75.



Freehand compression over breast phantom

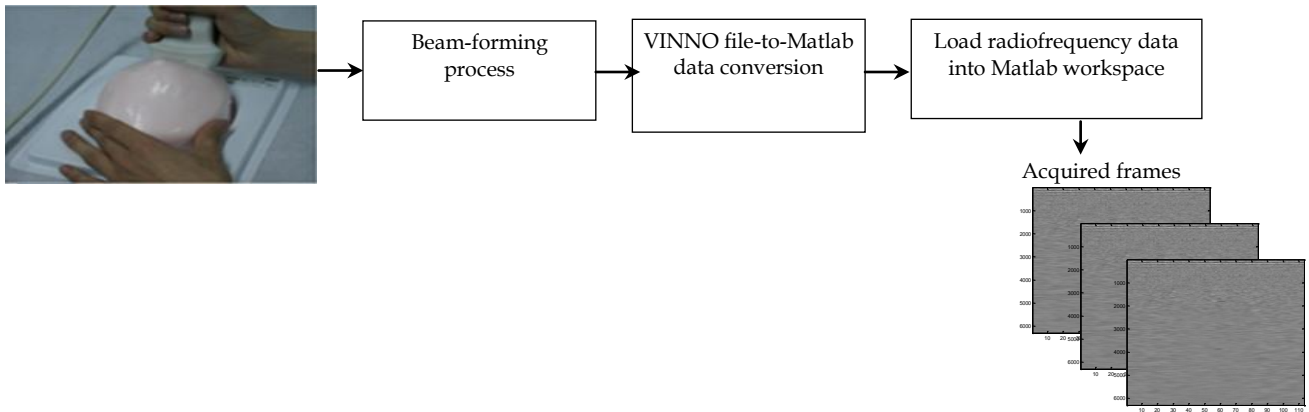


Fig. 1 Block daigram of experiment set-up

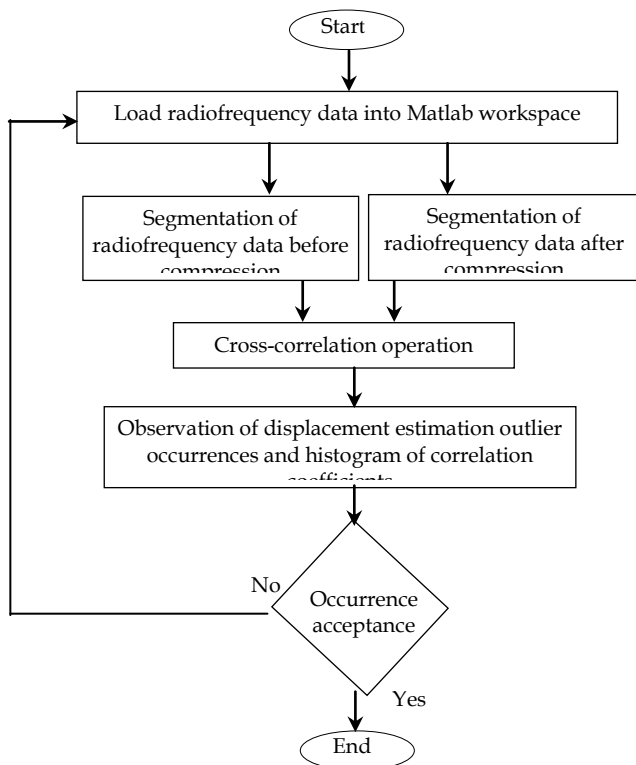


Fig. 2 Flowchart of optimal window length adjusment

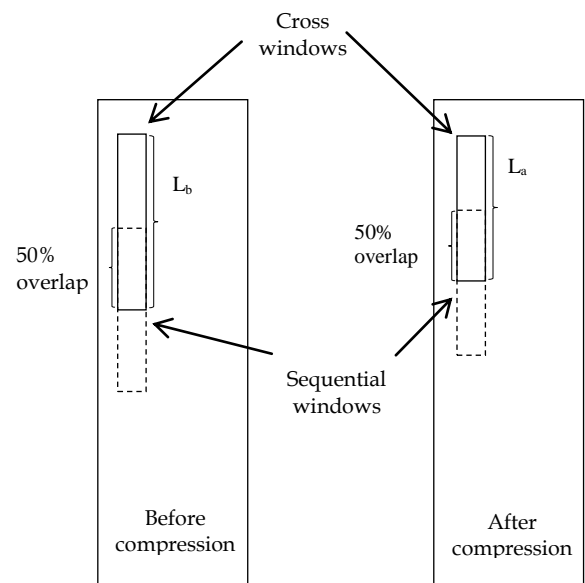


Fig. 3 Frame segmentation by sequential windows of before and after applied compression [18]



### 3. RESULTS AND DISCUSSION

The correlation parameters of before compression window length denoted by  $V_1$ , after compression window length factor denoted by  $F$ , correlation window over lapping denoted by  $W$ , where they are adjusted, for  $V_1$  as 40, 60, 80, 120, 140 axial samples, for  $F$  as 1, 1.1, 1.2, 1.3, 1.4, and for  $W$  as 0.25, 0.5, 0.75. In estimated -mated displacement map, outlier occurrences denoted by  $C$  and measured within the region of  $n$  of interest (ROI) at different correlation parameters, as illustrated in Tables(1, 2, and 3). - and 3). Results illustrate that when  $V_1$  increased from 100-140 the outlier occurrence decreases significantly, this is due to the fact that similarity between the before and after compression windows increases. Although that, axial resolution decreases when window length increases.

On the other hand the Tables (1, 2, and 3) illustrate that  $F$  that at  $F$  at 1.1 decreases the outlier occurrences significantly, where its considered in this research as an optimal value. As a consequence, for displacement map at higher axial resolution of  $V_1$  at 40 samples and  $F$  at 1.1 ratio, sequential overlapping of  $W$  at 0.75 illustrates lower outlier occurrence is shown in figure(4).Figure(4-a,b) shows a reduction of outlier occurrences at an expense of axial resolution. While, Figure(4-c, d, e, f) shows how the outlier occurrences affected by correlation parameters.

In addition, median filter of 3-by-3 dimension is also used to reduce the outlier occurrences that has been illustrated in tables (1,2 and 3). The median filter was previously used and considered as a non-linear operation and operated in non-supervised way [14]. So that the performance of median filter at different correlation parameters is shown in Figure(5), where outlier occurrences reduced significantly as shown in Figure(5-a, b, c, d, e, f). Particularly when diffuse occurrence of outliers at  $V_1$  of 100, 120, and 140

V1	40	60	80	100	120	140
F	1	1	1	1	1	1
W	0.25	0.25	0.25	0.25	0.25	0.25
C	18453	9964	5198	3180	1672	977
V1	40	60	80	100	120	140
F	1.1	1.1	1.1	1.1	1.1	1.1
W	0.25	0.25	0.25	0.25	0.25	0.25
C	7478	4526	2144	1262	718	408
V1	40	60	80	100	120	140
F	1.2	1.2	1.2	1.2	1.2	1.2
W	0.25	0.25	0.25	0.25	0.25	0.25
C	9342	5068	2396	1513	717	425
V1	40	60	80	100	120	140
F	1.3	1.3	1.3	1.3	1.3	1.3
W	0.25	0.25	0.25	0.25	0.25	0.25
C	10383	5661	3201	1816	1109	601
V1	40	60	80	100	120	140
F	1.4	1.4	1.4	1.4	1.4	1.4
W	0.25	0.25	0.25	0.25	0.25	0.25
C	11770	6792	4171	2559	1399	850

Figure(5- d, e, f). Otherwise, some other outliers at specular occurrence still exist as shown in Figure(5-a,b,c), where median filter not robust enough to refine.

**Table (1):** Correlation window length ( $V_1=40-80$ ), post window factor ( $F=1-1.4$ ) and correlation window overlapping ( $W=0.25$ )

V1	40	60	80	100	120	140
F	1	1	1	1	1	1
W	0.5	0.5	0.5	0.5	0.5	0.5
C	15443	8527	4150	2866	1557	773
V1	40	60	80	100	120	140
F	1.1	1.1	1.1	1.1	1.1	1.1
W	0.5	0.5	0.5	0.5	0.5	0.5
C	6366	3840	2079	1276	701	341
V1	40	60	80	100	120	140
F	1.2	1.2	1.2	1.2	1.2	1.2
W	0.5	0.5	0.5	0.5	0.5	0.5
C	8451	4510	2399	1585	708	574
V1	40	60	80	100	120	140
F	1.3	1.3	1.3	1.3	1.3	1.3
W	0.5	0.5	0.5	0.5	0.5	0.5
C	9483	5211	2887	1795	1125	889
V1	40	60	80	100	120	140
F	1.4	1.4	1.4	1.4	1.4	1.4
W	0.5	0.5	0.5	0.5	0.5	0.5
C	6552	4007	2114	1284	701	367

**Table (2):** Correlation window length ( $V_1=40-80$ ), post window factor ( $F=1-1.4$ ) and correlation window overlapping ( $W=0.5$ )

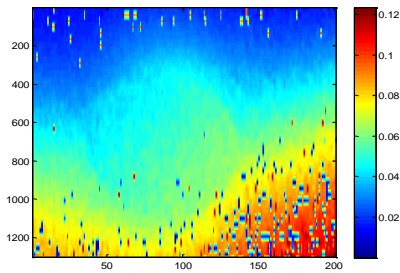
**Table (3):** Correlation window length ( $V_1=40-80$ ), post window factor ( $F=1-1.4$ ) and correlation window overlapping ( $W=0.75$ )

V1	40	60	80	100	120	140
F	1	1	1	1	1	1
W	0.75	0.75	0.75	0.75	0.75	0.75
C	15112	7250	3646	1551	1257	481
V1	40	60	80	100	120	140
F	1.1	1.1	1.1	1.1	1.1	1.1
W	0.75	0.75	0.75	0.75	0.75	0.75
C	5759	3523	2193	717	198	581
V1	40	60	80	100	120	140
F	1.2	1.2	1.2	1.2	1.2	1.2
W	0.75	0.75	0.75	0.75	0.75	0.75
C	7995	4002	2337	890	409	835
V1	40	60	80	100	120	140
F	1.3	1.3	1.3	1.3	1.3	1.3
W	0.75	0.75	0.75	0.75	0.75	0.75
C	14369	10940	7770	4615	2260	2370
V1	40	60	80	100	120	140
F	1.4	1.4	1.4	1.4	1.4	1.4
W	0.75	0.75	0.75	0.75	0.75	0.75
C	21562	18156	13496	8763	4959	3346

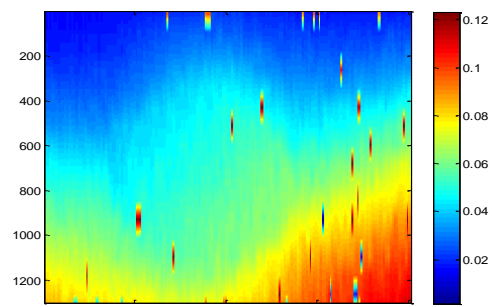


Axial samples

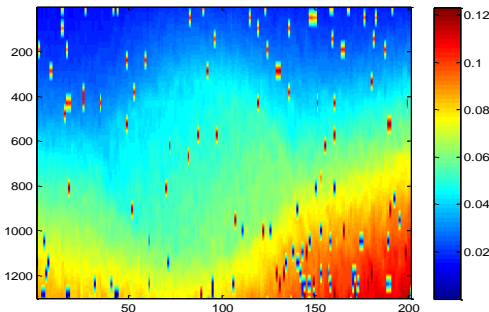
Displacement



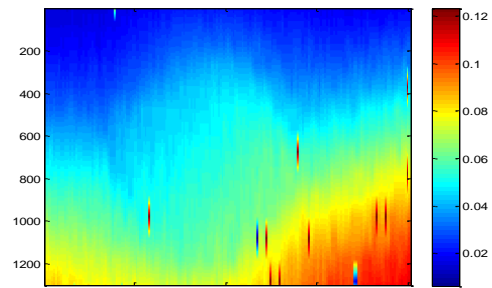
Lateral lines  
(a)



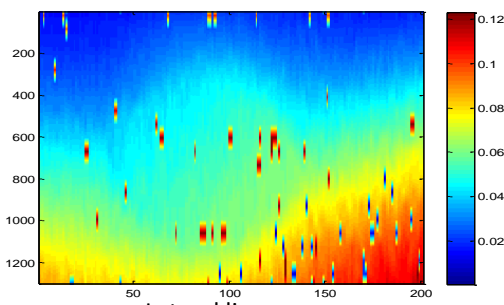
(d)



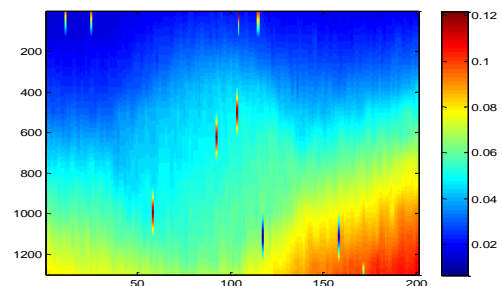
Lateral lines  
(b)



(e)

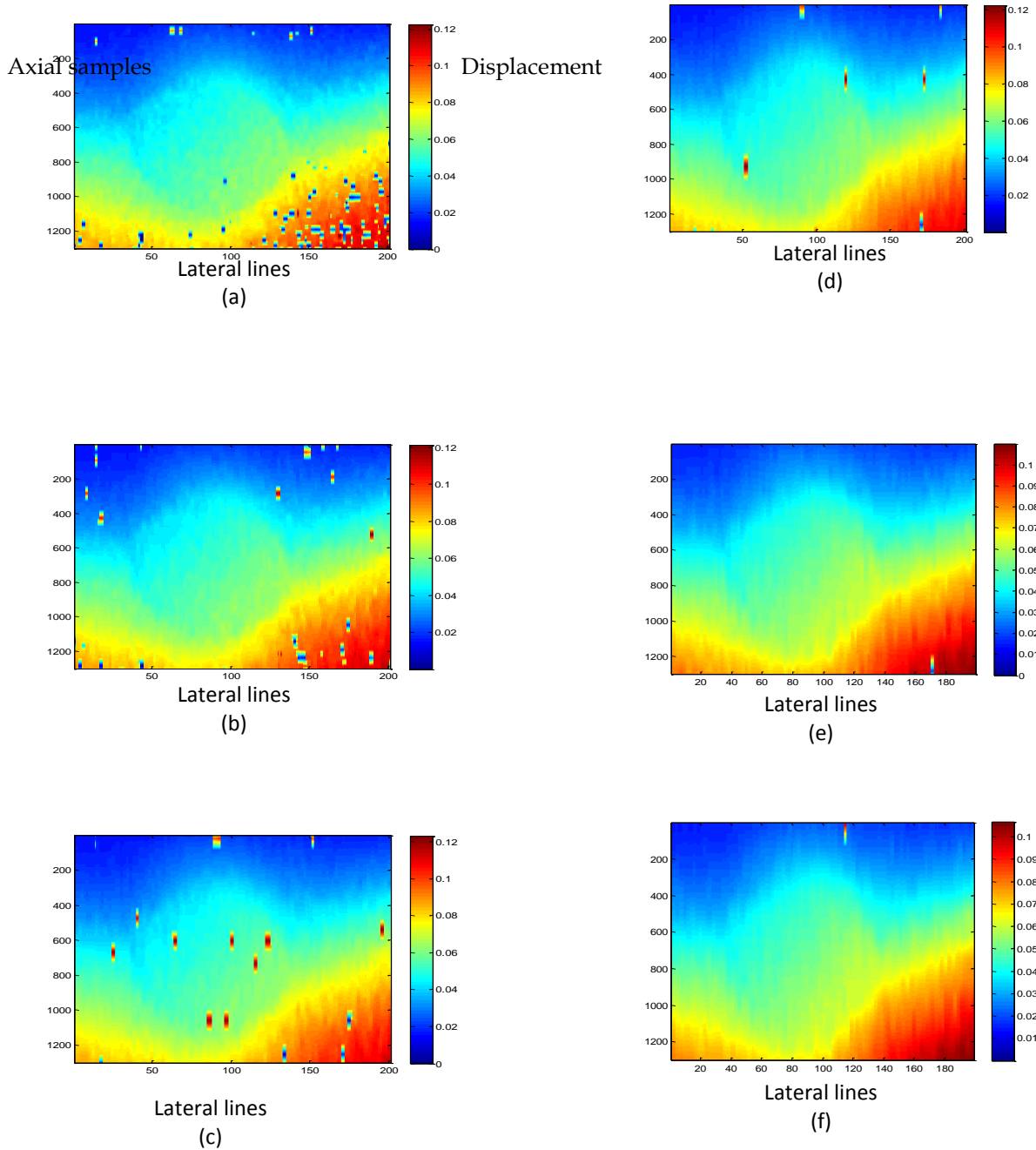


(c)



Lateral lines  
(f)

Fig(4) Displacement map at different correlation parameters as: (a)  $V_1=40$ ,  $F=1.1$ ,  $W=0.75$ ,  $C=5759$ , (b)  $V_1=60$ ,  $F=1.1$ ,  $W=0.75$ ,  $C=3523$ , (c)  $V_1=80$ ,  $F=1.1$ ,  $w=0.75$ ,  $C=2193$  (d)  $V_1=100$ ,  $F=1.1$ ,  $W=0.75$ ,  $C=717$ , (e)  $V_1=120$ ,  $F=1.1$ ,  $W=0.75$ ,  $C=198$  (f)  $V_1=140$ ,  $F=1.1$ ,  $W=0.75$ ,  $C=581$ .



Figure(5) 3-by-3 median filter that reduces the outlier occurrences, (a)  $V_1=40, F=1.1, W=0.75, C=1549$ , (b)  $V_1=60, F=1.1, W=0.75, C=926$ , (c)  $V_1=80, F=1.1, w=0.75, C=395$  (d)  $V_1=100, F=1.1, W=0.75, C=218$ , (e)  $V_1=120, F=1.1, W=0.75, C=66$  (f)  $V_1=140, F=1.1, W=0.75, C=106$ .



#### 4. CONCLUSION

In this research, a localization of breast phantom inclusion differentiated based on displacement map estimation. Displacement map was estimated using similarity measurement algorithm of cross-correlation at optimally adjusted correlation parameters. Results showed estimation outlier occurrences can be reduced at certain axial resolution at the optimal correlation parameters. 3-by-3 median filter also considered to reduce outliers and to measure median filter robustness against outlier occurrences. Although median filter able to reduce outlier occurrences, but some other outliers were still exist particularly at small window length of before applied compression (specular outlier occurrence at certain regions) at an expense of reduction of displacement map spatial resolution. Supervised linear algorithm is recommended to reduce outlier occurrence as an alternative to the median filter.

#### 5. REFERENCES

- [1] World Health Organisation, "Cancer burden rises to 18.1 million new cases and 9.6 million cancer deaths in 2018," *Int. Agency Res. cancer*, no. September, pp. 13–15, 2018.
- [2] R. S. Khandpur, *Automated drug delivery systems*. 2003.
- [3] J. Enderle, S. Blanchard, and J. Bronzino, *Introduction to Biomedical Engineering*. 2005.
- [4] James E. Moore Jr. Duncan J. Maitland, 'Biomedical Technology and Devices', Taylor & Frances Group, 2<sup>nd</sup> Ed, 2014.
- [5] R. G. P. (Richard G. P. Lopata, *2D and 3D ultrasound strain imaging: methods and in vivo applications*. 2010.
- [6] U. Techavipoo, Q. Chen, T. Varghese, J. A. Zagzebski, and E. L. Madsen, "Noise reduction using spatial-angular compounding for elastography," *IEEE Trans. Ultrason. Ferroelectr. Freq. Control*, vol. 51, no. 5, pp. 510–520, 2004.
- [7] P. Chaturvedi, M. F. Insana, and T. J. Hall, "2-D companding for noise reduction in strain imaging," *IEEE Trans. Ultrason. Ferroelectr. Freq. Control*, vol. 45, no. 1, pp. 179–191, 1998.
- [8] M. F. Insana, P. Chaturvedi, T. J. Hall, and M. gBilgen, "3-D companding using linear arrays for improved strain imaging," pp. 1435–1438, 2002.
- [9] S. K. Alam, J. Ophir, and E. E. Konofagou, "An adaptive strain estimator for elastography," *IEEE Trans. Ultrason. Ferroelectr. Freq. Control*, vol. 45, no. 2, pp. 461–472, 2002.
- [10] A. Sayed, G. Layne, J. Abraham, and O. Mukdadi, "Nonlinear characterization of breast cancer using multi-compression 3D ultrasound elastography in vivo," *Ultrasonics*, vol. 53, no. 5, pp. 979–991, 2013.
- [11] T. Liang, L. Yung, and W. Yu, "On Feature Motion Decorrelation in," vol. 32, no. 2, pp. 435–448, 2013.
- [12] H. S. Hashemi, M. Boily, P. A. Martineau, and H. Rivaz, "Ultrasound elastography: efficient estimation of tissue displacement using an affine transformation model," *Med. Imaging 2017 Ultrason. Imaging Tomogr.*, vol. 10139, p. 1013903, 2017.
- [13] M. Ghasemi Amidabadi, M. Omair Ahmad, and H. Rivaz, "Supervised Classification of the Accuracy of the Time Delay Estimation in Ultrasound Elastography," *IEEE Trans. Ultrason. Ferroelectr. Freq. Control*, vol. 65, no. 1, pp. 21–29, 2018.
- [14] A. Al-azawi, J. Dziejewicz, J. Soraghan, S. Inglis, and A. Gachagan, The First International Conference for Engineering Researches "Ultrasound Elastography : Performance Evaluation of Displacement Field Refinement Process for Freehand Compression" no. March, 2017.
- [15] T. H. E. Perfect, D. Tool, and F. O. R. Sonoelastography, "the Perfect Demonstration Tool for Sonoelastography," no. 1, 2013.
- [16] M. Ashfaq, S. S. Brunke, J. J. Dahl, H. Ermert, C. Hansen, and M. F. Insana, "An ultrasound research interface for a clinical system," *IEEE Trans. Ultrason. Ferroelectr. Freq. Control*, vol. 53, no. 10, pp. 1759–1770, 2006.
- [17] "VINNO Transducer Specification Ultrasound System Transducers," pp. 5–7.
- [18] A. Alazawi, "On Ultrasound Elastography : Simulation, Experiment, and Algorithm Development" PhD dissertation. University of Strathclyde, Declaration of Authenticity and Author's Rights", no. June, 2015.





## Maximum Torque Per Ampere Considering different IPMSM Drive parameters

Farah Mazin Salim, Hanan Mikhael D. Habbi.

<sup>1</sup>Department of Electrical Engineering, University of Baghdad

---

### ABSTRACT

Interior Permanent magnet synchronous motor is used in different applications like HEV's due to its attractive characteristics from small size to high efficiency and high-power density. PMSM is an ordinary A.C machine and in order to control this machine different control algorithms such as constant V/F, field-oriented control and direct torque control are used. In this paper, maximum torque per ampere (MTPA) strategy is used to control the torque of a PMSM that can be used as a contributing parameter in the above-mentioned control algorithms.

---

### KEYWORDS

IPMSM drive motor, Maximum torque per ampere control, Speed control, field-oriented control, Matlab-Simulink.

---

### NOMENCLATURES

$i_{sd}, i_{sq}$  d and q axis currents, A.  
 $V_{sd}, V_{sq}$  d and q axis voltages, V.  
 $R_s$  stator resistance,  $\Omega$   
 $\omega_e$  synchronous electrical speed, rad/sec  
 $\psi_q, \psi_d$  d and q axis flux linkages, Wb  
 $\psi_m$  flux linkage of the PM, Wb.  
 $P_b$  pole pair, unitless.

---

### ARTICLE INFO

Received 9 May 2019

Accepted 20 June 2019

DOI: 10.xxxxx

ISSN: 2413-0230

AL-MUHANDIS Journal (JMISE)

© 2018 Iraqi Society of Engineers (ISE)

E-mail: [jmise@ise-iq.org](mailto:jmise@ise-iq.org)

Online: [www.jmise.ise-iq.org](http://www.jmise.ise-iq.org)

Office Address: Iraq, Baghdad, Al-Nidhal Q., 103-30-5

---

### CORRESPONDING AUTHOR

Name: Farah Mazin Salim

Email: [farahsakura77@gmail.com](mailto:farahsakura77@gmail.com)

Research Field: Electrical Engineering

Google Scholar: None

## 1. INTRODUCTION

Interior permanent magnet synchronous motor has gained so much attention in the past few years due to its attractive characteristics [1-2]. From small size to high efficiency and high-power density which makes it a good candidate to be used in hybrid electric vehicles (HEV'S) From all the types of electrical machines permanent magnet synchronous machines enjoy high efficiency and torque density since the permanent magnets can generate substantial air gap magnetic flux without external excitation. This special trait has enabled PMSM to be an excellent candidate in many motor drive applications.

IPMSM has two operating regions. The first region is the constant torque region in which the speed of the motor is below the base speed and the second region is the region where the speed of the motor is above the base speed which is called the flux-weakening region. The first region uses the MTPA control strategy to ensure that the required torque is produced with minimum stator current to reduce the machine copper losses and by doing this the overall efficiency of the motor is improved [3-4]. In this paper a MTPA based on derivation of the stator direct axis current control strategy is used for two different motor parameters in which the (d) and (q) inductances are varied to see its effect called the flux-weakening region [5-6]. The variation of  $L_d$  and  $L_q$  with respect to the component currents  $i_d$ ,  $i_q$  is illustrated. The simulation results are verified by using Matlab / Simulink considering different PMSM parameters.

## 2. Mathematical Model of IPMSM

The  $V_{sd}$  and  $V_{sq}$  voltage equations of IPMSM are given by the following equations [7]:

$$V_{sd} = R_s \cdot i_{sd} + \frac{d\psi_d}{dt} - \omega_e \psi_q \quad (1)$$

$$V_{sq} = R_s \cdot i_{sq} + \frac{d\psi_q}{dt} + \omega_e \psi_d \quad (2)$$

To which:

$$\psi_d = L_d i_{sd} + \psi_m \quad (3)$$

$$\psi_q = L_q i_{sq} \quad (4)$$

The motor torque is calculated using the following equation:

$$T_e = \frac{3}{2} \cdot P_b \cdot (\psi_m \cdot i_{sq}) + \frac{3}{2} \cdot P_b \cdot (L_d - L_q) \cdot i_{sd} i_{sq} \quad (5)$$

The electromagnetic torque has two terms, the first term is produced by the intersection between the stator current and the permanent magnet flux linkage which is called the reluctance torque. The second term is due to the saliency of the motor. In this paper the effect of the magnetic saturation is not considered and hence both ( $L_d$ ) and ( $L_q$ ) are both considered to be constant [3]. In the next step the MTPA is calculated based on the equations (1-5) [8].

## 3. MTPA control

This control strategy works on generating the required torque value by using minimum stator current. The copper losses of the machine are reduced and the efficiency of the machine is increased [4].

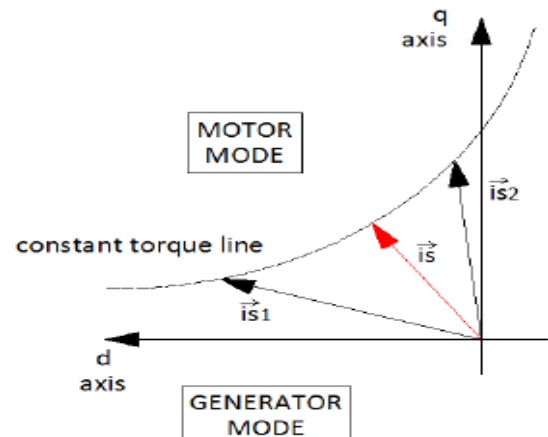


Figure 1. – currents in d-q axes

Figure (1) shows that for a given torque level there are different possibilities of stator current vectors represented by ( $i_{s1}$ ,  $i_{s2}$ ) that can give the required torque level but the vector with the red color represents the stator current vector gives the minimum current that can produce the same required torque level [9]. The starting point in finding MTPA is to use the torque equation given in the equation (5): But there are concentrations needs to be taken under consideration:

$$I_{smax}^2 = i_{sd}^2 + i_{sq}^2 \quad (6)$$

Where,

$I_{smax}$  is the maximum amplitude of the current Supplied by the inverter. To find ( $i_{sd}$ ) min that satisfies the torque equation,  $T_e$  is derived with respect to  $i_{sd}$  :



$$\frac{dT_e}{di_{sd}} = \frac{3}{2} P_b \cdot \frac{-i_{sd} \psi_m + (L_d - L_q)(I_{smax}^2 - 2i_{sd}^2)}{\sqrt{I_{smax}^2 - i_{sd}^2}}$$

$$2i_{sd}^2 + \frac{\psi_m}{(L_d - L_q)} i_{sd} - I_{smax}^2 = 0$$

$$\therefore i_{sd} = \frac{-\psi_m + \sqrt{\psi_m^2 + 8(L_d - L_q)^2 I_{smax}^2}}{4(L_d - L_q)} \tag{7}$$

And  $I_{sq}$  is calculated:

$$i_{sq} = \sqrt{I_{smax}^2 - i_{sd}^2} \tag{8}$$

Equations (5), (7) and (8) are the main three equations used to determine the MTPA.

**4. RESULTS:**

A MATLAB m-file was conducted in order to generate the required MTPA curve and for two different PMSM drive parameters. The first motor has the parameters tabulate in Table 1:

Table 1. IPMSM parameters

Parameters	value	unit
Stator resistance		
$R_s$	9.62	mΩ
d axis inductance $L_d$	28.7	μH
q-axis inductances $L_q$	47.2	μH
No of pole pair		
$P_b$	6	-
PM flux linkage		mwb
$\psi_m$	9.71	

The MTPA curve came out as shown in Figure 2 showing the effect of variation of  $i_d$  with respect to  $i_q$ , whereas Figure 3 shows the MTPA of different values of  $L_d$  and Figure 4 illustrates the MTPA of different values of  $L_q$ .

Figure 2. MTPA curve

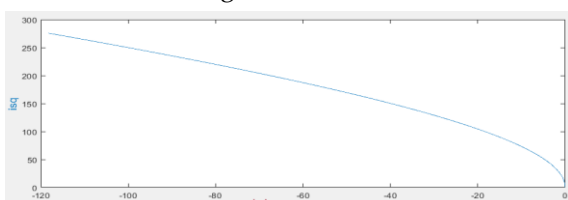


Figure 3. MTPA of different values of  $L_d$

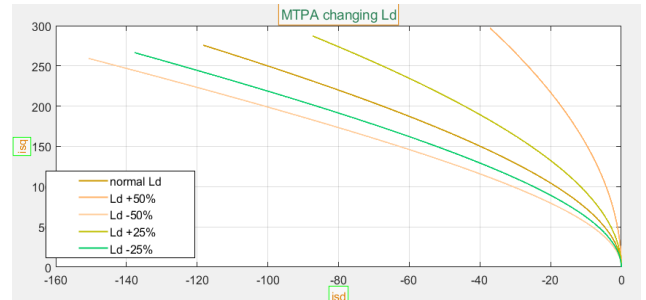


Figure 4. MTPA of different values of  $L_q$

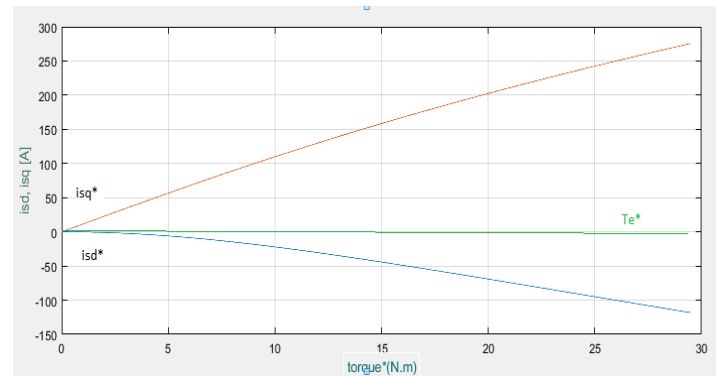


Figure 5. Generation of the current commands  $i_{sd}^*$ ,  $i_{sq}^*$  from the torque reference

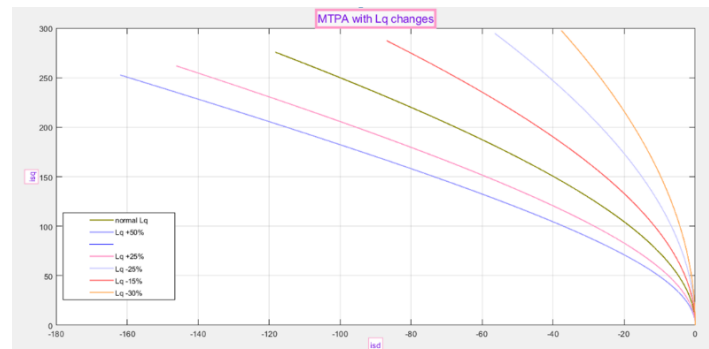




Table 2. IPMSM parameters

Parameters	value	unit
Stator resistance $R_s$	0.22	$\Omega$
d axis inductance $L_d$	3.3	mH
q-axis inductances $L_q$	31.2	mH
No of pole pair $P_b$	2	-
PM flux linkage $\psi_m$	0.116	mwb

The simulation results came out as shown in Figures 6, 7, and 8:

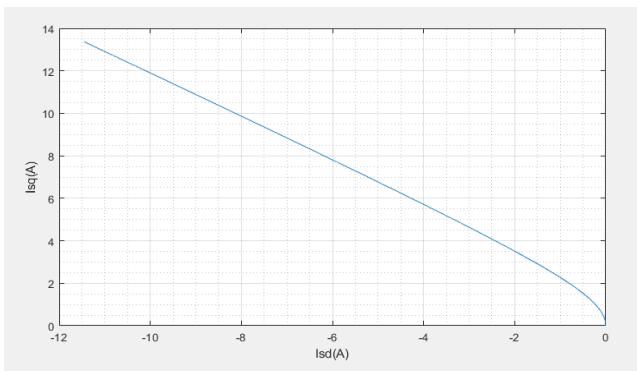


Figure 6. MTPA curve for the second motor parameter

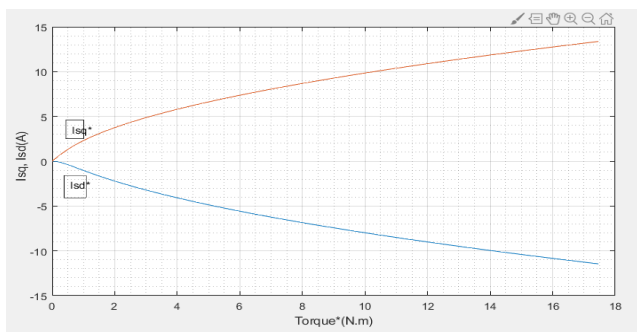


Figure 7. Generation of the current commands  $i_{sd}^*$ ,  $i_{sq}^*$  from the torque reference

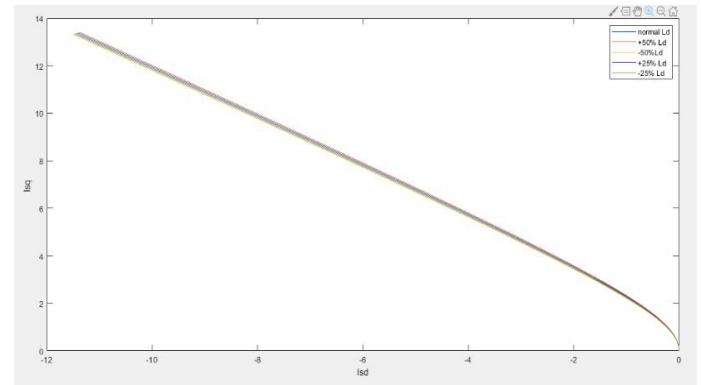


Figure. 8 - MTPA for  $L_d$  changes.

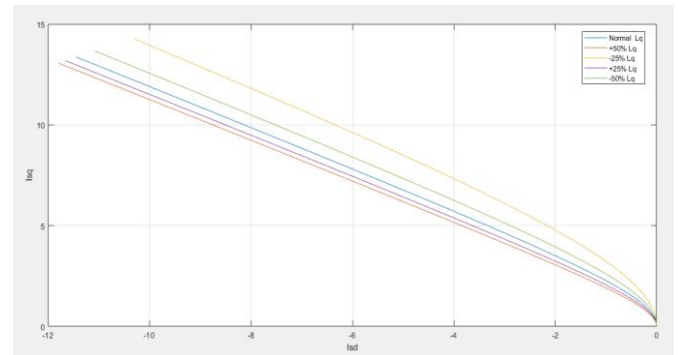


Figure. 9 - MTPA for  $L_q$  changes

Figure 2 and 6 shows the typical curve shape for the MTPA. Figure 3 ,4 ,8 and 9 shows how the maximum torque per ampere change when  $L_d$  and  $L_q$  change in certain percentages .There is a positive and negative increase in the values of  $L_d$  and  $L_q$  and it is noticed that when there is a positive change in  $L_d$ . the curve is increasing and when there is a negative change the curve is decreasing this means that  $i_d$  and  $i_q$  currents drawn are changing depends. increments and decrements.



## 5 . Conclusion:

The figures shown in this paper represent how the MTPA curve is drawn for different PMSM drive parameters. It can be concluded that, for the variations of  $L_q$  things are quite different when there is a positive change the curve decreases and when there is a negative change the curve increases. Figure 5 and 7 shows how to generate current commands from the MTPA curve so that they can be used in different control strategies such as FOC.

## 6.REFERENCES:

- [1] Ching-Tsai Pan, and Shinn - Ming Sue, " A linear maximum torque per ampere control for IPMSM drives over full speed range," IEEE transaction on Energy Conversion, vol.20, No.2, June 2005.
- [2] Rahman MA, Zhou, P. Field circuit analysis of brushless permanent magnet synchronous motors. IEEE Transactions on Industry Electronics. 1996; 43(2): 256-267.
- [3] P.D. Chandana P,: Sensorless control of PMSM drives, IET Alborg University, PhD. Thesis, Dec, 2002.
- [4] T.M.Jahns G.B.Kliman: Interior Permanent-Magnet Synchronous Motors for Adjustable-Speed Drives, IEEE Transactions On Industry Applications, Vol. IA-22, No.4, pp. 738-747. Jul/ Aug 1986.
- [5] Tao Zhou, Qing Liang Liu: Flux-weakening method for permanent magnet synchronous motor by lead-angle control, Appliance Technology, 2003, pp.61-64.
- [6] Xu Zhang , Guoqiang Zhang , Bo Wang , Yong Yu , Jing Zhang , and Dianguo Xu, "Maximum Torque Increase and Performance Optimization for Induction Motor Field-Weakening Control", 2018 21st International Conference on Electrical Machines and Systems (ICEMS), Jeju, Korea,.October 7-10, 2018,
- [7] Jun Li, Qinruo Wang, Jiajun Yu, Jianbin Xiong," Field-weakening Control Algorithm for Interior Permanent Magnet Synchronous Motor Based on Space-Vector Modulation Technique", Journal of Convergence Information Technology (JCIT), Volume8, Number3, Feb 2013.
- [8] Shoudao Huang, Ziqiang Chen, Keyuan Huang, and jian Gao," Maximum torque per ampere and flux weakening control for PMSM based on curve fitting" , IEEE conference on vehicle power and proposition, 2010.
- [9] Morimoto S, Takeda Y, Hirasa T, Taniguchi K: "Expansion of operating limits for permanent magnet motor by current vector control considering inverter capacity", IEEE Tran. on Ind. Application, vol. 26, pp. 886-871, Sept/Oct 1990.

